

Infrared properties of the quark-gluon vertex in general kinematics

A. C. Aguilar,¹ M. N. Ferreira,^{2,3} G.T. Linhares,¹ B. M. Oliveira,¹ and J. Papavassiliou^{4,5}

¹*University of Campinas - UNICAMP, Institute of Physics Gleb Wataghin,
13083-859 Campinas, São Paulo, Brazil.*

²*School of Physics, Nanjing University, Nanjing, Jiangsu 210093, China*

³*Institute for Nonperturbative Physics,
Nanjing University, Nanjing, Jiangsu 210093, China*

⁴*Department of Theoretical Physics and IFIC,
University of Valencia and CSIC, E-46100, Valencia, Spain.*

⁵*ExtreMe Matter Institute EMMI, GSI,
Planckstrasse 1, 64291 Darmstadt, Germany*

Abstract

In the present work we determine the eight form factors of the transversely-projected quark-gluon vertex in general kinematics, in the context of Landau-gauge QCD with two degenerate light dynamical quarks. The study is based on the set of Schwinger-Dyson equations that govern the vertex form factors, derived within the formalism of the three-particle-irreducible (3PI) effective action. The analysis is performed by employing lattice data for the main ingredients, such as gluon and quark propagators, and three-gluon vertex. The numerical treatment is simplified by decoupling the system of integral equations: the classical form factor is determined from a single non-linear equation involving only itself, while the remaining ones are subsequently computed through simple integrations. The form factors are obtained for arbitrary values of space-like momenta, and their angular dependence is examined in detail. A clear hierarchy is established at the level of the corresponding dimensionless effective couplings, in agreement with results of earlier studies. Furthermore, the classical form factor is found to be in excellent agreement with recent unquenched lattice data in the soft-gluon configuration, while the two non-classical dressings depart substantially from the lattice results. Finally, the accurate implementation of multiplicative renormalizability is confirmed, and the transition from Minkowski to Euclidean space is elucidated.

I. INTRODUCTION

The quark-gluon vertex, $\Gamma_\mu(q, p_2, -p_1)$, is one of the key ingredients of Quantum Chromodynamics (QCD) [1], playing a central role in the dynamical breaking of chiral symmetry [2–5] and the attendant emergence of constituent quark masses [6–13], the formation of the bound states that comprise the physical spectrum [14–23], and the ongoing exploration of the phase diagram of the theory [24–29]. Given its paramount importance for contemporary hadron physics, the quark-gluon vertex has been studied extensively within perturbation theory [30–35], by means of continuous nonperturbative approaches [10–12, 19–21, 36–55], and through a plethora of lattice simulations [56–66].

An especially advantageous framework for studying the nonperturbative aspects of the quark-gluon vertex in the continuum is the formalism based on the effective action [67, 68], and particularly its three-particle irreducible (3PI) version, at the three-loop order [69–72], explored first in [45], and later in the broader study of [20]. One of the special characteristics of this formalism is that the resulting Schwinger-Dyson equation (SDE) for the quark-gluon vertex, also known as “equation of motion”, is composed of diagrams with all their fundamental vertices fully-dressed. This is to be contrasted with the standard SDE formulation, where one of the vertices is always kept at its classical (tree-level) form. There are two main implications stemming from this difference. First, the typical difficulty of dealing with diagrams multiplied by a renormalization constant (the one assigned to the vertex that has remained undressed) is bypassed, and the renormalization procedure becomes subtractive; for an alternative approach, see [12]. Second, the three-gluon vertex, which enters in the numerically dominant diagram, is fully-dressed; therefore, a firm grasp of its nonperturbative properties becomes indispensable for the successful implementation of this approach.

In the present work we revisit the SDE of the *transversely-projected* quark-gluon vertex within the 3PI approach, under the light of recent developments related to the infrared structure of the three-gluon vertex [73–77]. The importance of this special vertex for the dynamics of the quark-gluon vertex and the size of the constituent quark masses has been amply emphasized already in a series of articles [78–80]. Nonetheless, our understanding of the three-gluon vertex has advanced substantially in the last few years, thanks to the combined scrutiny carried out by continuum methods [73–75, 81–90] and large-volume lattice simulations [76, 77, 91–97]. The picture that has emerged may be summarized through the

following key features: (a) the form factor associated with the classical tensor displays a considerable suppression with respect to its tree-level value (unity), at intermediate and low momentum scales [73–77, 81–97]; (b) the pivotal property of “planar degeneracy” reduces substantially the kinematic complexity of this vertex [73–77], furnishing simple and accurate forms for it, which are easily implementable in complicated computations; and (c) the classical form factor diverges logarithmically in the deep infrared, as a consequence of the nonperturbative masslessness of the ghost propagator [81, 98–109].

There are certain key aspects of our analysis that need to be emphasized from the outset. To begin with, a considerable simplification is implemented through the effective decoupling of the vertex SDE from the dynamical equations that govern the evolution of all other correlation functions, including the gap equation of the quark propagator. In particular, we do not solve a system of coupled SDEs, but use instead lattice inputs for all elements entering into this SDE, with the exception of the quark-gluon vertex itself. Note in particular, that we use lattice ingredients for the $N_f = 2$ gluon [110, 111] and quark propagators [61, 112], and minor variations around the best fit to the $N_f = 2 + 1$ data for the three-gluon form factor [95]. In addition, the system of eight coupled integral equations is simplified by retaining in their kernels solely the dependence on the classical form factor, λ_1 , setting all others to zero. This gives rise to a single self-coupled integral equation for λ_1 ; when solved, the λ_1 found is substituted into the kernels of the remaining form factors, which are then obtained through simple integration.

The main results of this analysis include:

(i) The eight form factors of the transversely-projected quark-gluon vertex are computed for arbitrary values of the incoming space-like momenta.

(ii) The $\lambda_1(q, p_2, -p_1)$ displays a considerable dependence on the angle between the momenta p_1 and p_2 , while the non-classical form factors present a comparably milder dependence on this angle [46, 79].

(iii) The construction of a renormalization-group invariant (RGI) and dimensionless effective coupling for each form factor reveals a clear hierarchy amongst them, in qualitative agreement with the results of [10, 12, 46].

(vi) The infrared behaviour of λ_1 is particularly sensitive to variations of the gluon dressing function, while variations of the three-gluon vertex and the quark propagator have a lesser impact.

(*v*) The λ_1 in the soft-gluon limit shows excellent agreement with the lattice data of [61], with a 7% departure in the deep infrared, which can be further reduced through minimal adjustments of the three-gluon vertex dressing. However, the other two relevant form factors are very different from the lattice results.

The article is organized as follows. In Sec. II we introduce the notation and main ingredients, and discuss general features of the quark-gluon vertex. In Sec. III the relevant SDE is derived, and its renormalization is discussed. In Sec. IV we discuss the simplifications implemented and the inputs employed. Sec. V contains the main results of this work; most notably, a detailed study of the angular dependence of the form factors, and a comparison with the lattice data of [61]. Then, in Sec. VI we verify the multiplicative renormalizability of the SDE solution for the classical form factor. In Sec. VII we present our discussion and conclusions. Finally, in Appendix A we elaborate on the transformation rules between Minkowski and Euclidean space.

II. NOTATION AND MAIN INGREDIENTS

In this section, we introduce the notation and the main elements that are relevant for the ensuing considerations. Our discussion will be restricted to the case of *two degenerate light dynamical quarks*, denoted by $N_f = 2$. Note that the formal analysis is carried out in Minkowski space; for the purpose of the numerical treatment, some key formulas are then converted to Euclidean space, and are evaluated for space-like momenta.

The full quark-gluon vertex, represented diagrammatically in panel (a) of Fig. 1, is denoted by

$$\mathbb{\Gamma}_\mu^a(q, p_2, -p_1) = ig t^a \Gamma_\mu(q, p_2, -p_1), \quad (2.1)$$

where g is the gauge coupling, q and p_2 are the incoming gluon and quark momenta, $p_1 = q + p_2$ is the outgoing anti-quark momentum. In addition, t^a ($a = 1, 2, \dots, N^2 - 1$) are the generators of the group $SU(N)$ in the fundamental representation. The matrices t^a are hermitian and traceless, generating the closed algebra

$$[t^a, t^b] = i f^{abc} t^c, \quad (2.2)$$

where f^{abc} are the totally antisymmetric structure constants. In the case of $SU(3)$, we have that $t^a = \lambda^a/2$, where λ^a are the Gell-Mann matrices. At tree-level, the quark-gluon vertex

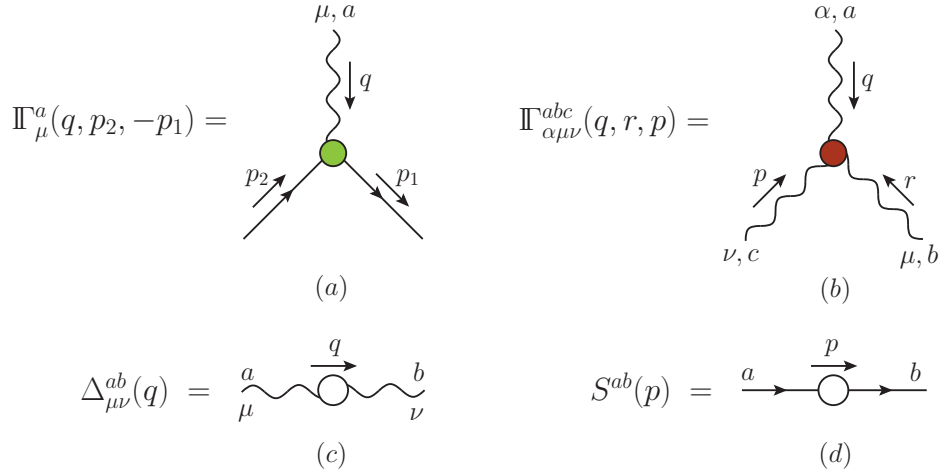


Figure 1. Diagrammatic representations of: (a) the full quark-gluon vertex, $\mathbb{\Gamma}_\mu^a(q, p_2, -p_1)$, defined in Eq. (2.1); (b) the full three-gluon vertex, $\mathbb{\Gamma}_{\alpha\mu\nu}^{abc}(q, r, p)$; (c) the fully-dressed gluon propagator, $\Delta_{\mu\nu}^{ab}(q)$; (d) the full quark propagator, $S^{ab}(p)$.

reduces to

$$\Gamma_0^\mu(q, p_2, -p_1) = \gamma^\mu. \quad (2.3)$$

The main focus of this study is the transversely-projected vertex, $\overline{\mathbb{\Gamma}}_\mu(q, p_2, -p_1)$, defined as

$$\overline{\mathbb{\Gamma}}_\mu(q, p_2, -p_1) := P_{\mu\nu}(q)\mathbb{\Gamma}^\nu(q, p_2, -p_1), \quad P_{\mu\nu}(q) := g_{\mu\nu} - q_\mu q_\nu / q^2. \quad (2.4)$$

Its tree-level expression, to be denoted by $\overline{\Gamma}_\mu^0(q, p_2, -p_1)$, is obtained from Eq. (2.4) through the substitution $\mathbb{\Gamma}^\nu(q, p_2, -p_1) \rightarrow \Gamma_0^\nu(q, p_2, -p_1)$.

In general kinematics, $\overline{\mathbb{\Gamma}}_\mu(q, p_2, -p_1)$ can be spanned by eight independent tensors, namely (Minkowski space)

$$\overline{\mathbb{\Gamma}}_\mu(q, p_2, -p_1) = \sum_{i=1}^8 \lambda_i(q, p_2, -p_1) P_{\mu\nu}(q) \tau_i^\nu(p_2, -p_1), \quad (2.5)$$

where the $\lambda_i(q, p_2, -p_1)$ denote scalar form factors, which depend on three Lorentz scalars. Even though several forms for the tensors τ_i^ν have been employed over the years, in the present analysis we opt for the basis put forth in [10, 12, 46]; as was shown therein, this basis has the advantages of being free of kinematic singularities and originating from gauge-

invariant operators. The elements of this basis in Minkowski space are given by

$$\begin{aligned}
\tau_1^\nu(p_2, -p_1) &= \gamma^\nu, & \tau_2^\nu(p_2, -p_1) &= (p_1 + p_2)^\nu, \\
\tau_3^\nu(p_2, -p_1) &= (\not{p}_1 + \not{p}_2)\gamma^\nu, & \tau_4^\nu(p_2, -p_1) &= (\not{p}_1 - \not{p}_2)\gamma^\nu, \\
\tau_5^\nu(p_2, -p_1) &= (\not{p}_1 - \not{p}_2)(p_1 + p_2)^\nu, & \tau_6^\nu(p_2, -p_1) &= (\not{p}_1 + \not{p}_2)(p_1 + p_2)^\nu, \\
\tau_7^\nu(p_2, -p_1) &= -\frac{1}{2}[\not{p}_1, \not{p}_2]\gamma^\nu, & \tau_8^\nu(p_2, -p_1) &= -\frac{1}{2}[\not{p}_1, \not{p}_2](p_1 + p_2)^\nu.
\end{aligned} \tag{2.6}$$

It is important to emphasize that, when the τ_i^ν of Eq. (2.6) are rotated to Euclidean space following the procedure outlined in App. A, one recovers precisely the basis of [10], given in Eq. (A2). This coincidence, in turn, ensures the unambiguous correspondence (and with the correct signs) between our form factors and those of [10].

Notice that the full vertex, $\overline{\Pi}_\mu(q, p_2, -p_1)$, must obey the same transformation properties as the bare vertex under the charge conjugation operation C , namely [31, 32]

$$C\overline{\Pi}_\mu(q, p_2, -p_1)C^{-1} = -\overline{\Pi}_\mu^T(q, -p_1, p_2). \tag{2.7}$$

Then, interchanging the momenta $p_1 \leftrightarrow -p_2$ in the basis defined in Eq. (2.6), and using the fact that

$$C\gamma_\mu C^{-1} = -\gamma_\mu^T, \quad C[\gamma_\mu, \gamma_\nu]C^{-1} = [\gamma_\mu^T, \gamma_\nu^T], \tag{2.8}$$

we find that

$$\begin{aligned}
C\tau_i^\nu(p_2, -p_1)C^{-1} &= -[\tau_i^\nu(-p_1, p_2)]^T, & i &= 1, 2, 4, 6, 8, \\
C\tau_3^\nu(p_2, -p_1)C^{-1} &= [\tau_3^\nu(-p_1, p_2)]^T - 2[\tau_2^\nu(-p_1, p_2)]^T, \\
C\tau_5^\nu(p_2, -p_1)C^{-1} &= [\tau_5^\nu(-p_1, p_2)]^T, \\
C\tau_7^\nu(p_2, -p_1)C^{-1} &= -[\tau_7^\nu(-p_1, p_2)]^T - [\tau_5^\nu(-p_1, p_2)]^T,
\end{aligned} \tag{2.9}$$

up to terms proportional to q^ν (first equation, for $i = 4$, and last one), which vanish when contracted by $P_{\mu\nu}(q)$. Therefore, in order to satisfy Eq. (2.7), we must have

$$\begin{aligned}
\lambda_i(q, p_2, -p_1) &= \lambda_i(q, -p_1, p_2), & i &= 1, 4, 6, 7, 8, \\
\lambda_2(q, p_2, -p_1) + 2\lambda_3(q, p_2, -p_1) &= \lambda_2(q, -p_1, p_2), \\
\lambda_3(q, p_2, -p_1) &= -\lambda_3(q, -p_1, p_2), \\
\lambda_5(q, p_2, -p_1) - \lambda_7(q, p_2, -p_1) &= -\lambda_5(q, -p_1, p_2).
\end{aligned} \tag{2.10}$$

Combining the above relations with Lorentz invariance, which implies that the λ_i can only depend on the squares of the momenta, it follows that $\lambda_3(q, p_2, -p_1) = 0$, and $\lambda_7(q, p_2, -p_1) = 2\lambda_5(q, p_2, -p_1)$ when $p_1^2 = p_2^2$.

It is useful to separate the basis tensors into subsets that are either chirally symmetric (cs) or chiral symmetry breaking (csb): tensors with an odd (even) number of γ matrices belong to the set τ_{cs} (τ_{csb}). Specifically, we have

$$\tau_{cs} = \{\tau_1^\nu, \tau_5^\nu, \tau_6^\nu, \tau_7^\nu\}, \quad \tau_{csb} = \{\tau_2^\nu, \tau_3^\nu, \tau_4^\nu, \tau_8^\nu\}. \quad (2.11)$$

In the *Landau gauge* that we employ, the gluon propagator, $\Delta_{\mu\nu}^{ab}(q) = -i\delta^{ab}\Delta_{\mu\nu}(q)$, is fully transverse, *i.e.*,

$$\Delta_{\mu\nu}(q) = \Delta(q^2)P_{\mu\nu}(q), \quad \Delta(q^2) = \mathcal{Z}(q^2)/q^2, \quad (2.12)$$

where $\Delta(q^2)$ denotes the scalar component of the gluon propagator and $\mathcal{Z}(q^2)$ the corresponding dressing function. The diagrammatic representation of $\Delta_{\mu\nu}(q)$ is given in panel (c) of Fig. 1.

In addition, we denote by $S^{ab}(p) = i\delta^{ab}S(p)$ the quark propagator [see panel (d) of Fig. 1], whose standard decomposition is given by

$$S^{-1}(p) = A(p^2)\not{p} - B(p^2), \quad (2.13)$$

where $A(p^2)$ and $B(p^2)$ are the Dirac vector and scalar components, respectively. The dynamical quark mass function, $\mathcal{M}(p^2)$, is then defined as $\mathcal{M}(p^2) = B(p^2)/A(p^2)$. At tree-level,

$$S_0^{-1}(p) = \not{p} - m_q, \quad (2.14)$$

such that $A_0 = 1$ and $B_0 = m_q$, where m_q is the current quark mass.

Finally, we introduce the three-gluon vertex, $\mathbb{\Pi}_{\alpha\mu\nu}^{abc}(q, r, p) = gf^{abc}\mathbb{\Gamma}_{\alpha\mu\nu}(q, r, p)$, depicted in panel (b) of Fig. 1. At tree-level, $\mathbb{\Gamma}_{\alpha\mu\nu}(q, r, p)$ reduces to the standard expression

$$\Gamma_0^{\alpha\mu\nu}(q, r, p) = g^{\mu\nu}(r-p)^\alpha + g^{\alpha\nu}(p-q)^\mu + g^{\alpha\mu}(q-r)^\nu. \quad (2.15)$$

Note that, in our analysis, the three-gluon vertex is naturally contracted by three transverse projectors, namely

$$\overline{\mathbb{\Pi}}_{\alpha\mu\nu}(q, r, p) = P_\alpha^{\alpha'}(q)P_\mu^{\mu'}(r)P_\nu^{\nu'}(p)\mathbb{\Gamma}_{\alpha'\mu'\nu'}(q, r, p). \quad (2.16)$$

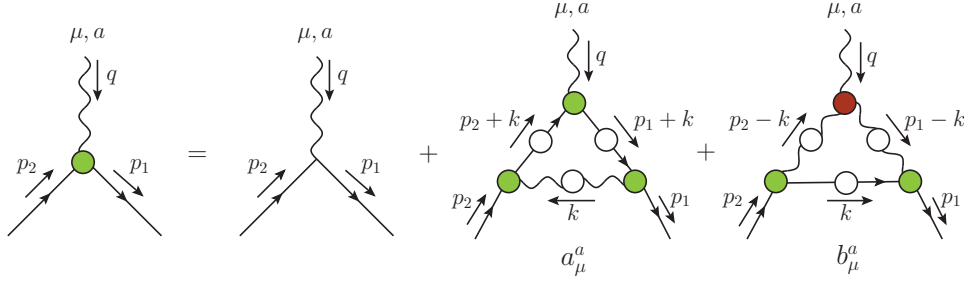


Figure 2. Diagrammatic representation of the SDE for the full quark-gluon vertex, $\mathbb{\Gamma}_\mu^a(q, p_2, -p_1)$, derived from the 3PI effective action at the three-loop level. White circles denote full propagators, and the green (red) circles denote the fully dressed quark-gluon (three-gluon)-vertices. Diagrams a_μ and b_μ are often referred to as “Abelian” and “non-Abelian”, respectively.

III. SDE OF THE QUARK-GLUON VERTEX

In this section we introduce the SDE of the quark-gluon vertex that will be employed in our analysis, and elaborate on the procedure adopted for its renormalization.

A. General structure

In this study, we employ the formulation of the quark-gluon SDE derived within the framework of the 3PI effective action [67, 68], at the *three-loop* level [20, 45, 69–72].

It is well-known that, within the n PI formalism, the SDE of a given Green’s function (also known as “equations of motion”) is obtained through the functional differentiation and subsequent extremization of the effective action with respect to the Green’s function in question. In the 3PI case, the relevant SDEs are derived from the effective action shown diagrammatically in Figs. 1-2 of [20, 69, 70]. At this level of approximation, all propagators (gluon, ghost, and quark) comprising this action are fully dressed, and so are the quark-gluon and three-gluon vertices; instead, the four-gluon vertex is kept at its tree-level value. Note also that the resulting propagator SDEs are “two-loop dressed”, while the vertex SDEs are “one-loop dressed”.

Specializing to the quark-gluon vertex, the corresponding SDE is diagrammatically depicted in Fig. 2. In particular, the transversely-projected quark-gluon vertex can be ex-

pressed in terms of the Abelian (a^μ) and non-Abelian (b^μ) diagrams as

$$\bar{\mathbb{I}}^\mu(q, p_2, -p_1) = \bar{\Gamma}_0^\mu(q, p_2, -p_1) + \bar{a}^\mu(q, p_2, -p_1) + \bar{b}^\mu(q, p_2, -p_1), \quad (3.1)$$

where

$$\bar{a}^\mu(q, p_2, -p_1) = P_\nu^\mu(q) a^\nu(q, p_2, -p_1), \quad \bar{b}^\mu(q, p_2, -p_1) = P_\nu^\mu(q) b^\nu(q, p_2, -p_1). \quad (3.2)$$

After carrying out the color algebra, the corresponding contributions in Minkowski space are given by

$$\begin{aligned} \bar{a}_\mu(q, p_2, -p_1) &= \kappa_a \int_k \Delta(k^2) \bar{\mathbb{I}}^\alpha(-k, k_1, -p_1) S(k_1) \bar{\mathbb{I}}_\mu(q, k_2, -k_1) S(k_2) \bar{\mathbb{I}}_\alpha(k, p_2, -k_2), \\ \bar{b}_\mu(q, p_2, -p_1) &= \kappa_b \int_k \Delta(\ell_1^2) \Delta(\ell_2^2) \bar{\mathbb{I}}_{\mu\alpha\beta}(q, \ell_1, -\ell_2) \bar{\mathbb{I}}^\alpha(-\ell_1, k, -p_1) S(k) \bar{\mathbb{I}}^\beta(\ell_2, p_2, -k), \end{aligned} \quad (3.3)$$

where $k_1 := k + p_1$, $k_2 := k + p_2$, $\ell_1 := k - p_1$, and $\ell_2 := k - p_2$, and we have introduced the factors

$$\kappa_a := -ig^2 \left(C_F - \frac{C_A}{2} \right), \quad \kappa_b := \frac{ig^2 C_A}{2}, \quad (3.4)$$

where C_F and C_A denote the eigenvalues of the Casimir operator in the fundamental and adjoint representations, respectively [$C_F = (N^2 - 1)/2N$ and $C_A = N$ for $SU(N)$].

Finally, we denote by

$$\int_k := \frac{1}{(2\pi)^4} \int d^4k, \quad (3.5)$$

the integration over virtual momenta, where the use of a symmetry-preserving regularization scheme is implicitly assumed.

It is straightforward to show that the expressions in Eq. (3.3) preserve charge conjugation symmetry; therefore, the form factors derived from these integrals automatically satisfy the constraints given in Eq. (2.10).

In order to derive the dynamical equations governing the form factors $\lambda_i(q, p_2, -p_1)$ in general kinematics, one has to construct a set of appropriate projectors, $\mathcal{P}_i^\mu(q, p_2, -p_1)$, satisfying the basic property

$$\text{Tr} [\mathcal{P}_i^\mu(q, p_2, -p_1) P_{\mu\nu}(q) \tau_j^\nu(p_2, -p_1)] = \delta_{ij}, \quad (3.6)$$

such that

$$\lambda_i(q, p_2, -p_1) = \text{Tr} [\mathcal{P}_{i\mu}(q, p_2, -p_1) \bar{\mathbb{I}}_R^\mu(q, p_2, -p_1)]. \quad (3.7)$$

The explicit construction of the projectors \mathcal{P}_i^μ proceeds by casting them in the form

$$\mathcal{P}_i^\mu(q, p_2, -p_1) = \sum_{j=1}^8 C_{ij}(p_2, -p_1) \tau_j^\mu(p_2, -p_1), \quad (3.8)$$

imposing Eq. (3.6), and solving the resulting system to determine the coefficients C_{ij} . This procedure yields

$$\begin{aligned} \mathcal{P}_1^\mu &= c_1 [4h\tau_1^\mu + r^2\tau_5^\mu - q^2\tau_6^\mu], & \mathcal{P}_5^\mu &= c_2 [4h(r^2\tau_1^\mu - 2\tau_7^\mu) + (3r^4 + 4h)\tau_5^\mu - 3r^2q^2\tau_6^\mu], \\ \mathcal{P}_2^\mu &= c_1 [q^2(\tau_2^\mu + \tau_3^\mu) - r^2\tau_4^\mu], & \mathcal{P}_6^\mu &= -c_2 [4hq^2\tau_1^\mu + 3q^2(r^2\tau_5^\mu - q^2\tau_6^\mu)], \\ \mathcal{P}_3^\mu &= c_1 [q^2(\tau_2^\mu - \tau_3^\mu) + r^2\tau_4^\mu], & \mathcal{P}_7^\mu &= -2c_1 [\tau_5^\mu + 2\tau_7^\mu], \\ \mathcal{P}_4^\mu &= c_1 [r^2(\tau_3^\mu - \tau_2^\mu) - (p_1 + p_2)^2\tau_4^\mu - 2\tau_8^\mu], & \mathcal{P}_8^\mu &= -4c_2 [2h\tau_4^\mu + 3q^2\tau_8^\mu], \end{aligned} \quad (3.9)$$

where we suppressed the argument $(q, p_2, -p_1)$ in the \mathcal{P}_i^μ and τ_i^μ , and introduced the definitions

$$r^2 := p_1^2 - p_2^2, \quad h := p_1^2 p_2^2 - (p_1 \cdot p_2)^2, \quad c_1 := 1/32h, \quad c_2 := 1/128h^2. \quad (3.10)$$

The SDE of Eq. (3.1) may be expressed in terms of the individual $\lambda_i(q, p_2, -p_1)$. To that end, it is convenient to denote by \mathbb{A}_i and \mathbb{B}_i the contributions arising from the contraction of the Abelian and non-Abelian diagrams in Fig. (2) by the projectors \mathcal{P}_i^μ , namely

$$\begin{aligned} \mathbb{A}_i(q, p_2, -p_1) &:= \text{Tr} \left[\mathcal{P}_{i\mu}(q, p_2, -p_1) \bar{a}^\mu(q, p_2, -p_1) \right], \\ \mathbb{B}_i(q, p_2, -p_1) &:= \text{Tr} \left[\mathcal{P}_{i\mu}(q, p_2, -p_1) \bar{b}^\mu(q, p_2, -p_1) \right]. \end{aligned} \quad (3.11)$$

Then, using Eqs. (3.6) and (3.7) it is easy to arrive at the system

$$\lambda_i(q, p_2, -p_1) = \delta_{i1} + \mathbb{A}_i(q, p_2, -p_1) + \mathbb{B}_i(q, p_2, -p_1), \quad i = 1, \dots, 8. \quad (3.12)$$

B. Renormalization

We next turn to the renormalization of the SDE for the quark-gluon vertex. Clearly, all quantities appearing in Eq. (3.1) are bare; the conversion to their renormalized counterparts is carried out multiplicatively, using the standard relations [1]

$$\begin{aligned} \Delta_R(q^2) &= Z_A^{-1} \Delta(q^2), & S_R(p) &= Z_F^{-1} S(p), & g_R &= Z_g^{-1} g, \\ \Pi_R^{\alpha\mu\nu}(q, r, p) &= Z_3 \Pi^{\alpha\mu\nu}(q, r, p), & \Pi_R^\mu(q, p_2, -p_1) &= Z_1 \Pi^\mu(q, p_2, -p_1), \end{aligned} \quad (3.13)$$

where the subscript “ R ” denotes renormalized quantities, and Z_A , Z_F , Z_g , Z_3 , and Z_1 are the corresponding (cutoff-dependent) renormalization constants. In addition, we employ the exact relations

$$Z_g^{-1} = Z_1^{-1} Z_A^{1/2} Z_F = Z_3^{-1} Z_A^{3/2}, \quad (3.14)$$

which are imposed by the fundamental Slavnov-Taylor identities (STIs) [113, 114].

We point out that the renormalization constant of the quark current mass, usually denoted by Z_{m_q} , has been omitted in Eq. (3.13). To be sure, in a self-contained SDE analysis, where the quark propagator is determined by its own SDE, the inclusion of Z_{m_q} would be indispensable. Indeed, in such a treatment, the current mass would appear explicitly in the quark SDE through the tree-level quark propagator, see Eq. (2.14); then, upon renormalization, Z_{m_q} would enter in the system of SDEs. Instead, in the present work we will employ renormalized lattice inputs for the external ingredients of Eq. (3.1). Then, since Eq. (3.1) does not explicitly contain the quark current mass, its corresponding renormalization constant does not appear in our analysis. For further details on this subject, the reader is referred to [10, 22, 27–29, 39, 46, 115–117], and references therein.

By substituting the relations of Eq. (3.13) into (3.1), and using Eq. (3.14), we readily obtain the renormalized version of (3.1), expressed as

$$\overline{\Pi}_R^\mu(q, p_2, -p_1) = Z_1 \overline{\Gamma}_0^\mu(q, p_2, -p_1) + \overline{a}_R^\mu(q, p_2, -p_1) + \overline{b}_R^\mu(q, p_2, -p_1), \quad (3.15)$$

where the subscript “ R ” in \overline{a}_R^μ and \overline{b}_R^μ indicates that the expressions provided in Eq. (3.3) have been replaced by their renormalized counterparts, as defined in Eq. (3.13). Then, from Eq. (3.15) one may readily derive the renormalized analog of Eq. (3.12), namely

$$\lambda_{i,R}(q, p_2, -p_1) = Z_1 \delta_{i1} + \mathbb{A}_{i,R}(q, p_2, -p_1) + \mathbb{B}_{i,R}(q, p_2, -p_1), \quad i = 1, \dots, 8. \quad (3.16)$$

Note that, due to the fact that all vertices comprising the diagrams \overline{a}^μ and \overline{b}^μ are fully-dressed, no renormalization constants appear multiplying them in Eq. (3.15). In fact, the only renormalization constant that survives in Eq. (3.15), namely Z_1 , is multiplying the tree-level contribution, thus converting the procedure of renormalization into subtractive instead of multiplicative. This is one of the main advantages offered by the 3PI formulation [20, 45, 71, 72], bringing about a major operational simplification.

To determine Z_1 we employ a variation of the momentum subtraction (MOM) scheme [118, 119], the so-called $\widetilde{\text{MOM}}$ scheme [57]. In particular, denoting by $\lambda_1^{sg}(p^2) := \lambda_1(0, p, -p)$

the classical form factor of the quark-gluon vertex in the soft-gluon limit ($q \rightarrow 0$), this particular scheme is defined by the prescriptions

$$\Delta_R^{-1}(\mu^2) = \mu^2, \quad A_R(\mu^2) = 1, \quad \lambda_{1,R}^{sg}(\mu^2) = 1. \quad (3.17)$$

The implementation of this condition at the level of Eq. (3.16) proceeds by considering the case $i = 1$ and taking the limit $q \rightarrow 0$. Employing the notation $\mathbb{A}_{i,R}(0, p, -p) := \mathbb{A}_{i,R}^{sg}(p^2)$ and $\mathbb{B}_{i,R}(0, p, -p) := \mathbb{B}_{i,R}^{sg}(p^2)$, we find

$$\lambda_{1,R}^{sg}(p^2) = Z_1 + \mathbb{A}_{1,R}^{sg}(p^2) + \mathbb{B}_{1,R}^{sg}(p^2). \quad (3.18)$$

Then, by imposing the renormalization condition of Eq. (3.17), we find

$$Z_1 = 1 - \mathbb{A}_{1,R}^{sg}(\mu^2) - \mathbb{B}_{1,R}^{sg}(\mu^2). \quad (3.19)$$

Thus, substituting Eq. (3.19) into Eq. (3.16), we arrive at the renormalized version of Eq. (3.16), namely

$$\lambda_{i,R}(q, p_2, -p_1) = [1 - \mathbb{A}_{i,R}^{sg}(\mu^2) - \mathbb{B}_{i,R}^{sg}(\mu^2)]\delta_{i1} + \mathbb{A}_{i,R}(q, p_2, -p_1) + \mathbb{B}_{i,R}(q, p_2, -p_1). \quad (3.20)$$

From now on the index “ R ” will be suppressed, to avoid notational clutter.

The SDEs in Eq. (3.20) will be solved under certain simplifying assumptions that we discuss in detail in the next section.

IV. NUMERICAL SETUP AND INPUTS

In this section we discuss the basic simplifications imposed on Eq. (3.20), derive its Euclidean version, and provide inputs for the propagators and vertices that comprise the terms \mathbb{A}_i and \mathbb{B}_i .

A. Simplifications

To reduce the algebraic complexity of this system, we approximate all transversely-projected quark-gluon vertices appearing on the rhs of Eq. (3.3) by retaining only their classical tensorial structures. Specifically, we set

$$\overline{\Pi}_\mu(q, p_2, -p_1) \rightarrow \lambda_1(q, p_2, -p_1)P_{\mu\nu}(q)\gamma^\nu. \quad (4.1)$$

Notice that implementing this approximation leads to two major simplifications: (i) the dynamical equation for the classical form factor, $\lambda_1(q, p_2, -p_1)$, decouples from the seven remaining form-factors, and (ii) the equation for the remaining form factors, $\lambda_i(q, p_2, -p_1)$ for $i \neq 1$, are expressed in terms of only λ_1 . Therefore, $\lambda_1(q, p_2, -p_1)$ is described by an integral equation, whereas the remaining λ_i are expressed in terms of ordinary integrals involving the form factor λ_1 .

Regarding the three-gluon vertex, we retain only its tree-level tensorial structure, and resort to the planar degeneracy approximation for the associated form factor, which has been validated by a series of studies [73–77]. Specifically, $\bar{\Pi}^{\mu\alpha\beta}(q, \ell_1, -\ell_2)$ can be accurately approximated by the compact form

$$\bar{\Pi}^{\mu\alpha\beta}(q, \ell_1, -\ell_2) = L_{sg}(s^2)\bar{\Gamma}_0^{\mu\alpha\beta}(q, \ell_1, -\ell_2), \quad s^2 = \frac{1}{2}(q^2 + \ell_1^2 + \ell_2^2), \quad (4.2)$$

where $\bar{\Gamma}_0^{\mu\alpha\beta}(q, \ell_1, -\ell_2) = P_{\mu'}^\mu(q)P_{\alpha'}^\alpha(\ell_1)P_{\beta'}^\beta(\ell_2)\Gamma_0^{\mu'\alpha'\beta'}(q, \ell_1, -\ell_2)$, with $\Gamma_0^{\mu'\alpha'\beta'}$ denoting the three-gluon vertex at tree-level given by Eq. (2.15). The function $L_{sg}(s^2)$ is the form factor associated with the soft-gluon limit of the three-gluon vertex, ($q = 0, \ell_1 = \ell_2$), and has been determined from various lattice simulations [76, 77, 91–96, 101].

B. Euclidean space

The conversion of Eq. (3.20) to Euclidean space proceeds by assuming that the external momenta are space-like, *e.g.*, $q^2 \rightarrow -q_E^2$ with $q_E^2 \geq 0$, and similarly for p_1 and p_2 . We then apply the following standard conversion rules

$$\Delta_E(q_E^2) = -\Delta(-q_E^2), \quad A_E(q_E^2) = A(-q_E^2), \quad B_E(q_E^2) = B(-q_E^2), \quad L_{sg}^E(q_E^2) = L_{sg}(-q_E^2), \quad (4.3)$$

and suppress the index “E” for simplicity.

In addition, it is convenient to employ hyperspherical coordinates, writing the integral measure as

$$\int_k \rightarrow \int_E = \frac{i}{16\pi^3} \int_0^\infty dz z \int_0^\pi d\phi_1 s_{\phi_1}^2 \int_0^\pi d\phi_2 s_{\phi_2}, \quad (4.4)$$

where $s_{\phi_1} := \sin \phi_1$. We then express all relevant form factors as functions of p_1^2, p_2^2 , and the angle between them, θ , namely

$$\lambda_i(q, p_2, -p_1) \rightarrow \lambda_i(p_1^2, p_2^2, \theta). \quad (4.5)$$

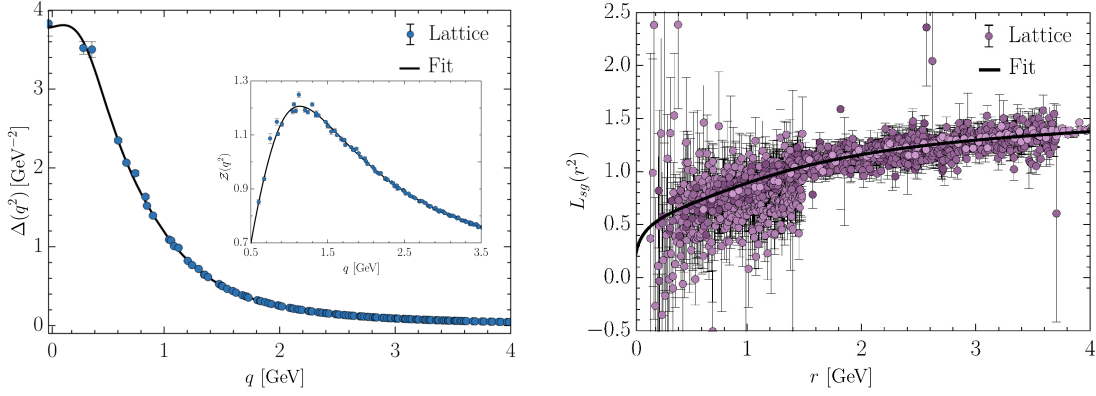


Figure 3. *Left panel:* The lattice data of [110, 111] for the gluon propagator, $\Delta(q^2)$, with $N_f = 2$ (points), together with the fit given by Eq. (A1) of [120] (black solid line). In the inset we show the gluon dressing function, $\mathcal{Z}(q^2)$, defined in Eq. (2.12). *Right panel:* Lattice data of [95] for $L_{sg}(r^2)$ with $N_f = 2 + 1$ (points), converted to the $\widetilde{\text{MOM}}$ scheme, which entails a rescaling by a factor of 1.16 [120]. The black continuous curve is the corresponding fit, given by Eq. (A1) of [120].

After implementing the above steps, we find that Eq. (3.16) assumes the schematic form

$$\lambda_i(p_1^2, p_2^2, \theta) = Z_1 \delta_{i1} + \int_{\text{E}} \mathcal{K}_{i\text{A}} \lambda_1^3 + \int_{\text{E}} \mathcal{K}_{i\text{B}} \lambda_1^2, \quad (4.6)$$

where $\mathcal{K}_{i\text{A}}$ and $\mathcal{K}_{i\text{B}}$ are the kernels of diagrams a_μ and b_μ in Fig. 2, respectively.

Moreover, in conformity with Eq. (3.19), the renormalization constant Z_1 is obtained as the soft-gluon limit of Eq. (4.6) for $i = 1$; specifically, setting $q = 0$, $p_1 = p_2 := p$, and $\theta = 0$, and subsequently fixing $p^2 = \mu^2$, we find

$$Z_1 = 1 - \lim_{q \rightarrow 0} \left[\int_{\text{E}} \mathcal{K}_{1\text{A}} \lambda_1^3 + \int_{\text{E}} \mathcal{K}_{1\text{B}} \lambda_1^2 \right]_{p^2 = \mu^2}. \quad (4.7)$$

C. Inputs

In what follows, the system of equations for the λ_i formed by Eqs. (4.6) and (4.7) are solved treating $\Delta(q^2)$, $A(p^2)$, $\mathcal{M}(p^2)$, and $L_{sg}(r^2)$ as external inputs.

(i) For $\Delta(q^2)$ we use a fit to the lattice data from [110, 111], with $N_f = 2$ (two degenerate light quarks), computed with current masses between 20 to 50 MeV, and pion masses ranging from 270 to 510 MeV. The functional form of this fit is provided in Eq. (A1) of [120], and is shown in the left panel of Fig. 3, together with the corresponding dressing function $\mathcal{Z}(q^2)$.

(ii) When dealing with the form factor $L_{sg}(r^2)$, additional care is needed, because, at present, there are no available lattice data for this quantity with $N_f = 2$. Given this limitation, we will employ a fit for lattice data with $N_f = 2 + 1$, which was used recently in the analysis of [120], see Eq. (A1) therein. Note that this simulation involves two light quarks with a current mass of 1.3 MeV, and a heavier one with a current mass of 63 MeV [95]. Moreover, the lattice results of [95] were originally computed in the so-called asymmetric MOM scheme, defined by the prescription $L_{sg}^{as}(\mu^2) = 1$. To employ them in our analysis, we convert them to the $\widetilde{\text{MOM}}$ scheme through the rescaling $L_{sg}(r^2) = 1.16L_{sg}^{as}(r^2)$, valid for $\mu = 2$ GeV, as determined in the Appendix B of [120].

In the right panel of Fig. 3 we show the $\widetilde{\text{MOM}}$ converted lattice data and the corresponding fit (black curve), denoted by $L_{sg}^*(r^2)$, which minimizes the χ^2 deviation from the data. The curve $L_{sg}^*(r^2)$ will serve as our reference input for $L_{sg}(r^2)$, *i.e.*, $L_{sg}(r^2) \rightarrow L_{sg}^*(r^2)$, for the bulk of our computations. However, minor variations from $L_{sg}^*(r^2)$ will be implemented in order to optimize the coincidence with the lattice data for λ_1 in the soft-gluon limit, and check the numerical stability of the entire procedure.

(iii) For the quark wave function, $1/A(p^2)$, and the corresponding dynamical mass, $\mathcal{M}(p^2)$, we employ fits for the setup denominated “L08” in the lattice simulation of [61, 112]. This simulation was performed for a current quark mass $m_q = 6.2$ MeV, and a pion mass $m_\pi = 280$ MeV. The functional forms of the fits for $A(p^2)$ and $\mathcal{M}(p^2)$ are given in Eqs. (A5) and (A6) of [120], respectively; these functional forms were adjusted to remove certain lattice artifacts in the ultraviolet, and to reproduce the respective one-loop resummed perturbative behaviour. Both the lattice data and the corresponding fits for $A(p^2)$ and $\mathcal{M}(p^2)$ are shown in Fig. 4.

(iv) All these inputs are renormalized in the $\widetilde{\text{MOM}}$ scheme defined by Eq. (3.17), at the renormalization point $\mu = 2$ GeV. For this particular μ we need to choose a value for $\alpha_s(\mu^2) := g^2(\mu^2)/4\pi$; whereas in [120] the estimate $\alpha_s(\mu^2) = 0.47$ was obtained by combining one-loop calculations and fits to lattice data, our SDE reproduces the lattice results for values of the strong charge in the vicinity of $\alpha_s(\mu^2) = 0.55$ (see next section).

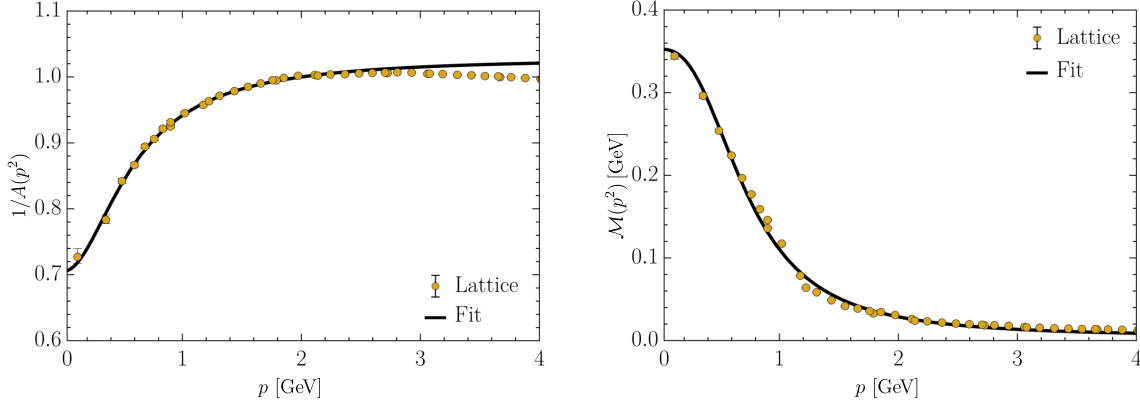


Figure 4. The lattice data (points) of [61, 112] for the quark wave function, $1/A(p^2)$ (left panel) and the running mass, $\mathcal{M}(p^2)$ (right panel), both corresponding to the “L08” setup. The fits (black solid lines) given by Eqs. (A4) and (A5) of [120] are also shown.

V. RESULTS

We next solve Eq. (4.6) for $i = 1$ iteratively, in order to obtain λ_1 . The integration is performed using a double-precision adaptive routine based on the Gauss-Kronrod integration rule [121]. The external momenta grid interval ranges logarithmically from $[10^{-3}, 10^3]$ GeV^2 , with 30 points, while the external angle grid is uniformly distributed across 10 points within the range $[0, \pi]$. The interpolations in three variables, needed for evaluating the λ_1 , are performed with B-splines [122]. Once λ_1 has been determined, we substitute it into Eq. (4.6) for $i = 2, \dots, 8$, and obtain all remaining λ_i through simple integration. In the rest of this Section, we present the main results of this analysis.

A. Classical (tree-level) form factor

In Fig. 5 we present numerical results for λ_1 , obtained from the iterative solution of Eq. (4.6). The results are displayed in four panels, each for a different value of θ . The diagonals of these plots ($p_1 = p_2$) are identified with the special kinematic configurations: (i) *soft-gluon*, blue curve; (ii) *totally symmetric*, red curve; (iii) *quark-symmetric*, brown curve; and (iv) *asymmetric*, yellow curve¹.

The sequence of all diagonals, obtained as the angle θ varies within the interval $[0, \pi]$, may

¹ Note that the value of θ in the totally symmetric configuration is not $2\pi/3$, since in our kinematics the antiquark momentum is outgoing.

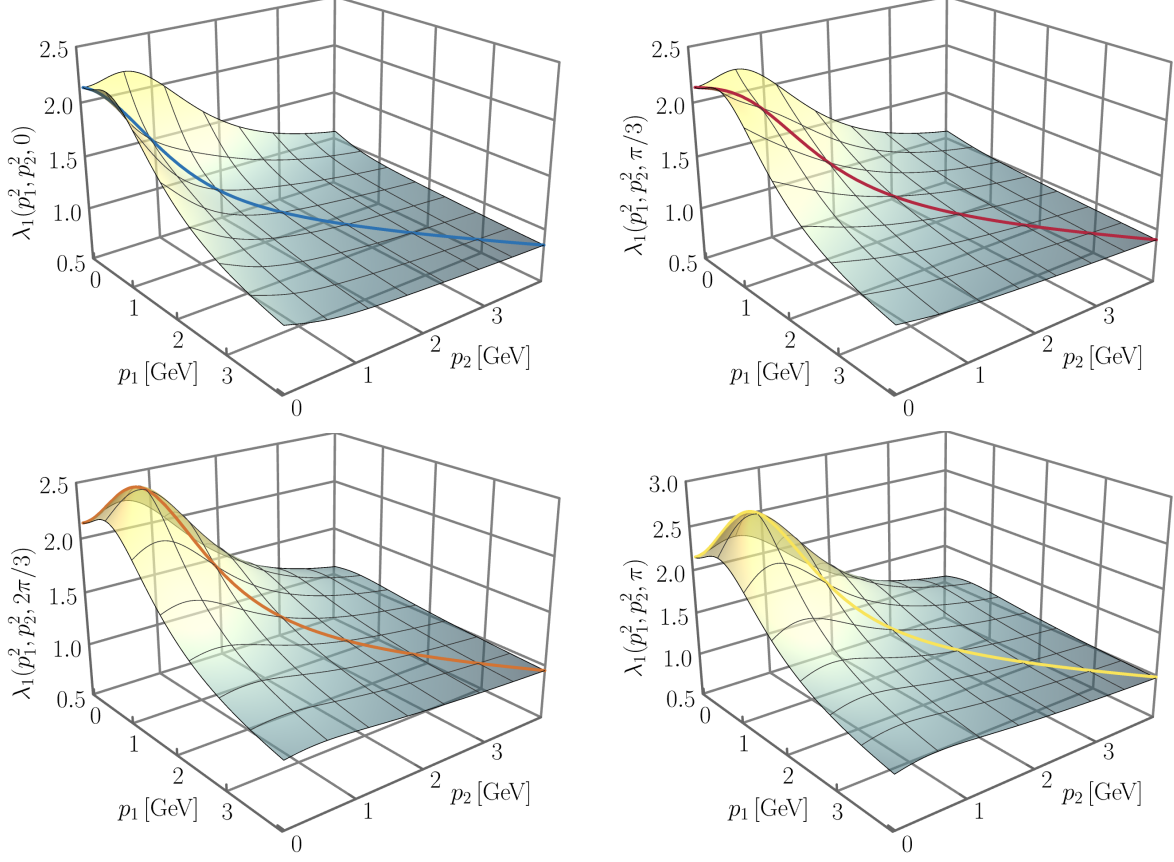


Figure 5. The form factor $\lambda_1(p_1^2, p_2^2, \theta)$ plotted as a function of the antiquark, p_1 , and quark, p_2 , momenta, for fixed angles $\theta = 0$ (upper left), $\theta = \pi/3$ (upper right), $\theta = 2\pi/3$ (lower left), and $\theta = \pi$ (lower right). Four kinematic limits are highlighted in the diagonals of each of the 3D surfaces: soft-gluon (blue), totally symmetric (red), quark-symmetric (brown), and asymmetric (yellow) configurations.

be plotted as a function of θ , giving rise to the collection of curves shown in the left panel of Fig. 6 [46, 79, 123]. The band is delimited by the soft-gluon and asymmetric configurations, $\theta = 0$ and $\theta = \pi$, respectively.

Clearly, as the angle θ increases, the peak of the form factors becomes more pronounced, in a continuous fashion. This pattern is displayed in the the right panel of Fig. 6, where the four aforementioned kinematic configurations are highlighted; note a 27% increase between the maxima of the soft-gluon and asymmetric configurations. For large values of the momentum, all curves decrease logarithmically, at the rate predicted in [32].

Note that the main contribution to this form factor stems from the non-Abelian diagram

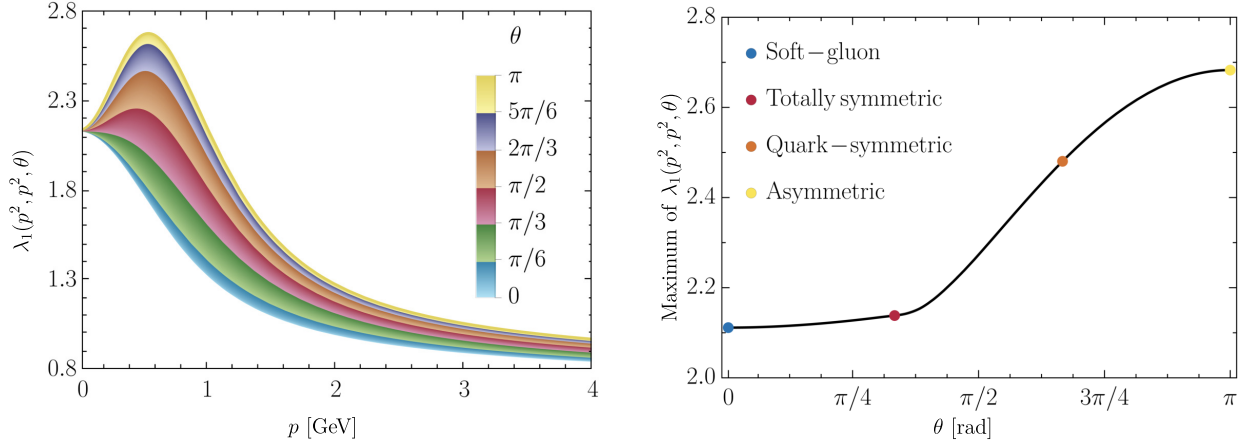


Figure 6. *Left panel:* The dependence of $\lambda_1(p_1^2, p_2^2, \theta)$ on the angle θ , when we set $p_1^2 = p_2^2 = p^2$. *Right panel:* The maximum value of the $\lambda_1(p^2, p^2, \theta)$ as a function of θ .

b_μ ; for instance, for the soft-gluon configuration, we have $\lambda_1^{sg}(0) = 2.138$, with $\mathbb{B}_{1,R}^{sg}(0) = 1.142$ and $\mathbb{A}_{1,R}^{sg}(0) = -0.004$, the rest (unity) coming from the tree-level contribution.

B. Non-classical form factors

Once the solution for $\lambda_1(p_1^2, p_2^2, \theta)$ in general kinematics is known, one may use it as input in Eq. (4.6) and determine the remaining form factors; in fact, each one of them is obtained through a single integration. The results for the chirally symmetric form factors λ_5 (upper left), λ_6 (upper right), λ_7 (lower) are shown in Fig. 7; while in Fig. 8, we present the results for the chiral symmetry breaking form factors λ_2 (upper left), λ_3 (upper right), λ_4 (lower left), λ_8 (lower right). In each of these figures, the corresponding form factor is plotted in terms of the momenta p_1 and p_2 , fixing the value of the angle at $\theta = 0$.

First, notice that the form factors λ_i with $i = 4, 6, 7, 8$ shown in Figs. 7 and 8 are symmetric with respect to the diagonal plane ($p_1 = p_2$) (blue or purple curves, respectively). This is a direct consequence of the charge conjugation symmetry satisfied by these form factors, as stated in Eq. (2.10). Observe that this property becomes visible in 3D surfaces only when $\lambda_i(p_1^2, p_2^2, \theta)$ is plotted as a function of the momenta p_1 and p_2 . In the case of λ_2 , this symmetry with respect to the diagonal is approximately satisfied, since λ_3 is very small, as shown in Fig. 8. The fourth relation in Eq. (2.10) is also satisfied numerically.

In addition, notice that the (blue or purple) continuous curves along the diagonals in

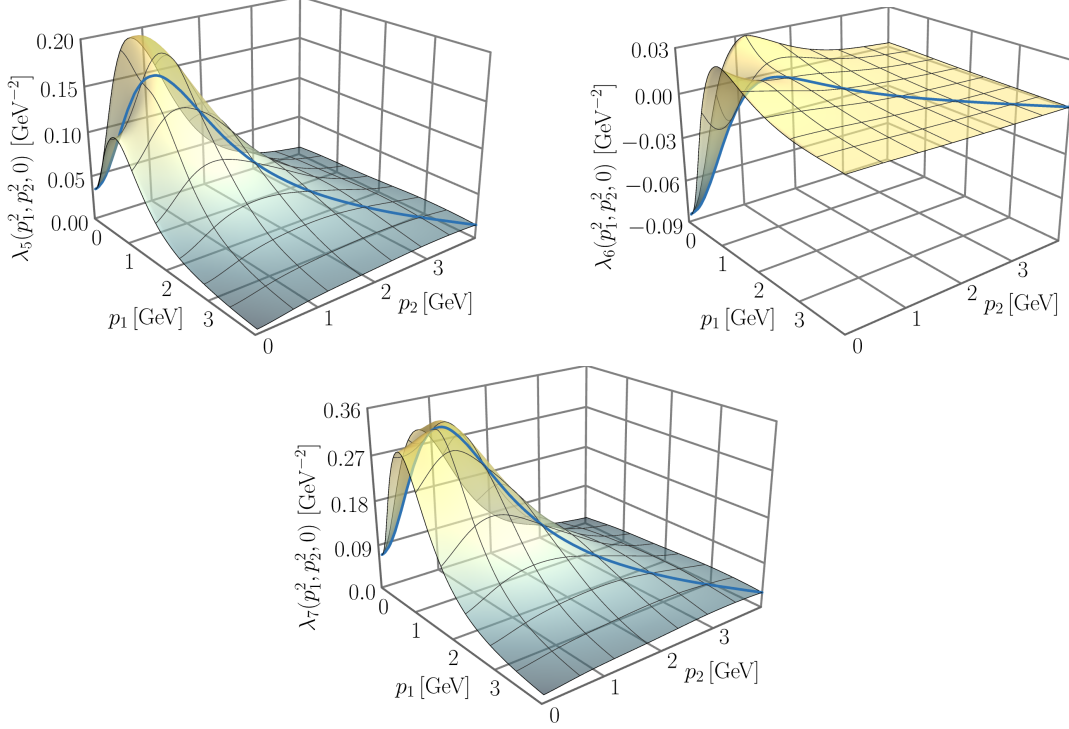


Figure 7. The chirally symmetric quark-gluon form factors $\lambda_i(p_1^2, p_2^2, \theta)$, with $i = 5, 6$ (upper row) and $i = 7$ (lower row) plotted as functions of the magnitudes of the momenta p_1 and p_2 , for a fixed value of the angle, $\theta = 0$. The blue curves along the diagonals represent the corresponding soft-gluon limits of each form factor.

these plots represent the corresponding soft-gluon limit of each form factor, since they are defined by the condition $p_1 = p_2$ or equivalently $q = 0$, and the angle was fixed at $\theta = 0$ in all panels.

In Fig. 9 we display the angular dependence of all non-classical form factors when $p_1^2 = p_2^2 = p^2$, with the exception of λ_3 , which is identically zero in this limit. As in the case of Fig. 6, all bands are delimited by the soft-gluon ($\theta = 0$) and asymmetric ($\theta = \pi$) configurations. It is evident that λ_2 and λ_8 exhibit the weakest angular dependence. In contrast, λ_4 and λ_6 show a slightly stronger dependence on θ , concentrated mainly in the momentum region where $p \leq 2$ GeV. Finally, λ_5 and λ_7 display a noticeably stronger dependence, practically in the entire range of momenta, although still milder than the angular dependence of λ_1 shown in Fig. 6.

As a general remark we point out that the non-classical form factors are infrared finite and depart considerably from their (vanishing) tree-level values, approaching their expected

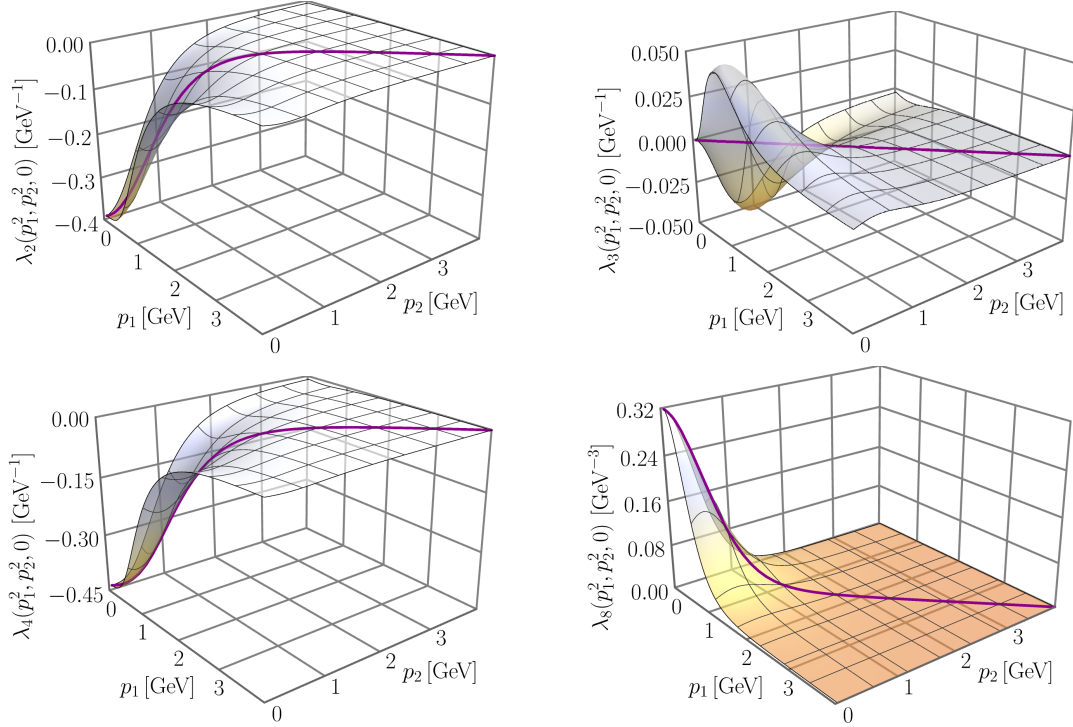


Figure 8. The chiral symmetry breaking quark-gluon form factors $\lambda_i(p_1^2, p_2^2, \theta)$, with $i = 2, 3$ (upper row) and $i = 4, 8$ (lower row) plotted as functions of the magnitudes of the momenta p_1 and p_2 , for a fixed value of the angle, $\theta = 0$. The purple curves along the diagonals represent the corresponding soft-gluon limit of each form factor.

perturbative behavior in the deep ultraviolet.

Note that the non-Abelian diagram dominates again numerically, especially in the cases of the form factors λ_2 and λ_4 , where its contribution exceeds the Abelian one by at least one order of magnitude.

C. The quark-gluon effective couplings

In order to carry out a meaningful comparison of the relative size of the various vertex form factors, it is advantageous to introduce dimensionless and RGI combinations, which serve as generalizations of the traditional effective couplings. Specifically, one singles out special kinematic configurations (*e.g.*, soft-gluon, totally symmetric, etc), where the λ_i depend on a single kinematic variable, and constructs a family of dimensionless effective couplings,

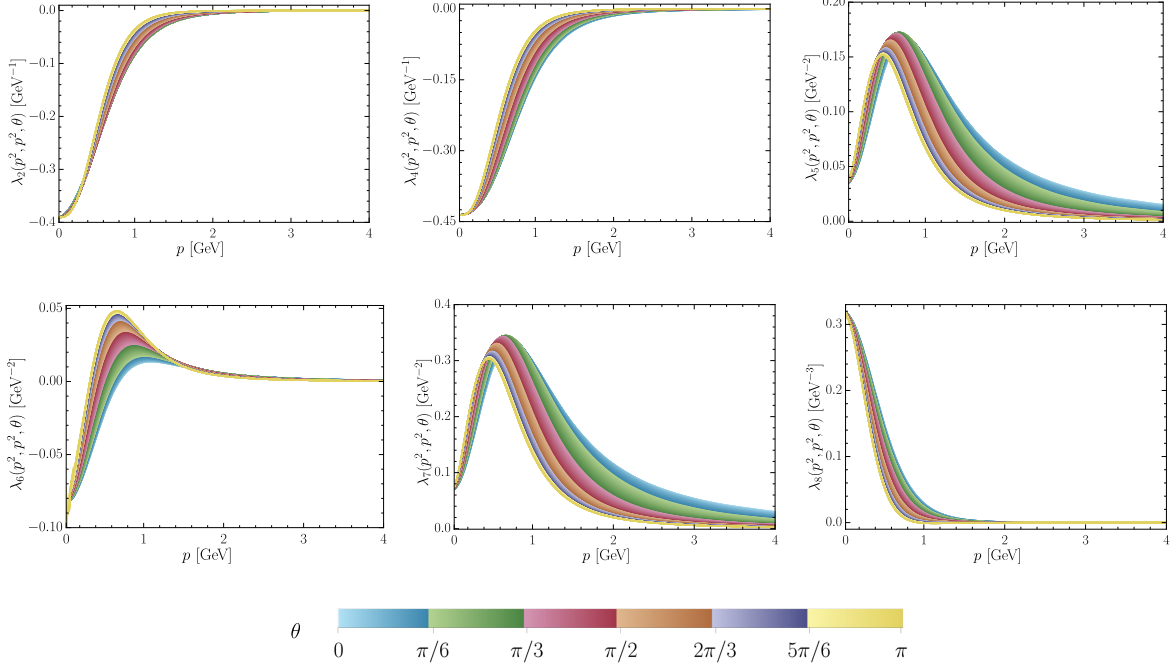


Figure 9. The angular dependence of the $\lambda_i(p_1^2, p_2^2, \theta)$ for $i = 2, 4, 5, 6, 7, 8$, for $p_1^2 = p_2^2 = p^2$.

$\widehat{g}_i(p^2)$, defined as [10, 12, 46, 91, 95]²

$$\widehat{g}_i(p^2) = g(\mu^2) [p^{n_i} \lambda_i(p^2)] A^{-1}(p^2) \mathcal{Z}^{1/2}(p^2), \quad \text{with } n_1 = 0, \quad n_{2,3,4} = 1, \\ n_{5,6,7} = 2, \quad n_8 = 3, \quad (5.1)$$

where $\mathcal{Z}(p^2)$ and $A(p^2)$ are defined in Eqs. (2.12) and (2.13), respectively.

In what follows we will choose as our special configuration the soft-gluon limit, whose form factors are given by the diagonals of the 3-D plots shown in Figs. 5, 7, and 8. We will therefore denote with the index “sg” the corresponding form factors and effective couplings, thus implementing into Eq. (5.1) the replacement

$$\widehat{g}_i(p^2), \lambda_i(p^2) \longrightarrow \widehat{g}_i^{sg}(p^2), \lambda_i^{sg}(p^2). \quad (5.2)$$

In Fig. 10 we present the results for $\widehat{g}_i^{sg}(p^2)$, separating them into two subsets, those associated with the τ_{cs} (left panel), and those related to the τ_{csb} (right panel), in accordance with the definition in Eq. (2.11). It is clear from Fig. 10 that the two groups of effective couplings satisfy the hierarchies

$$\widehat{g}_1^{sg}(p^2) > \widehat{g}_7^{sg}(p^2) > \widehat{g}_5^{sg}(p^2) > |\widehat{g}_6^{sg}(p^2)|, \quad |\widehat{g}_4^{sg}(p^2)| > |\widehat{g}_2^{sg}(p^2)| > \widehat{g}_8^{sg}(p^2). \quad (5.3)$$

² In [10, 12] the coupling $g(\mu^2)$ is included in the definition of the quark-gluon form factor λ_1 , whereas here it has been factored out, see Eq. (2.1).

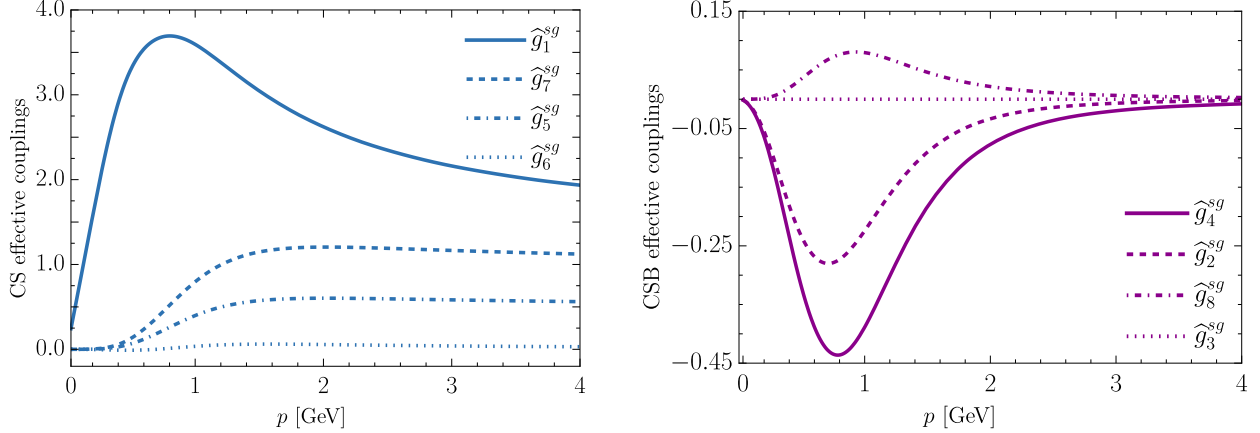


Figure 10. The quark-gluon effective couplings, $\widehat{g}_i^{sg}(p^2)$, for the chirally symmetric form factors $\lambda_{1,5,6,7}$ (left panel), and for the chiral symmetry breaking $\lambda_{2,3,4,8}$ (right panel). The effective couplings were determined from Eq. (5.1), with the $\lambda_i(p^2)$ in the soft-gluon kinematics.

Note that \widehat{g}_3^{sg} vanishes identically, and that $\widehat{g}_7^{sg}(p^2) = 2\widehat{g}_5^{sg}(p^2)$, manifesting the charge conjugation symmetry of the vertex [see discussion below Eq. (2.10)]. We have verified that the hierarchies given in Eq. (5.3) persist in the totally symmetric, quark-symmetric, and soft-gluon limits. Moreover, our results are in qualitative agreement with those presented in [10, 12, 46], where the effective couplings were computed in the totally symmetric configuration.

If we carry out the replacement $\lambda_1(p^2) \rightarrow \lambda_1(p^2, p^2, \theta)$ in the $\widehat{g}_1(p^2)$ of Eq. (5.1), we may obtain a continuous family of effective charges, $\alpha_{qg}(p^2, \theta)$, defined as [10, 46]

$$\alpha_{qg}(p^2, \theta) = \frac{\widehat{g}_1^2(p^2, \theta)}{4\pi}, \quad (5.4)$$

which are shown in Fig. 11. We note a considerable difference in size among the members of this family; in particular, the limiting cases $\theta = 0$ and $\theta = \pi$ are separated by a factor of 3 between peaks.

D. Varying the inputs

It is particularly important to acquire a quantitative understanding of how variations of the SDE inputs affect the final result. To that end, we perform small variations around the fits to lattice data used as inputs,³ and consider their impact on λ_1^{sg} .

³ In doing so, we keep the value of the strong charge fixed at $\alpha_s(\mu) = 0.55$.

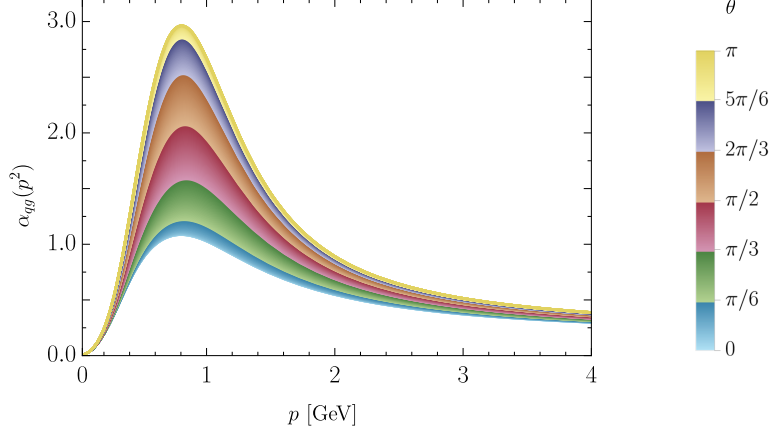


Figure 11. Family of effective charges extracted from the quark-gluon vertex, using different kinematic configurations for the classical form factor $\lambda_1(p^2, p^2, \theta)$.

Specifically, we solve Eq. (4.6) for λ_1^{sg} , each time substituting one input $f = [\Delta, L_{sg}, A, \mathcal{M}]$ by $f^\pm(p^2)$, where

$$\begin{aligned} \Delta^\pm(p^2) &= \Delta(p^2) \pm \delta_1/[1 + (p^2/\kappa_1^2)^2], & L_{sg}^\pm(p^2) &= L_{sg}^*(p^2) \pm \delta_2/[1 + (p^2/\kappa_2^2)^2], \\ 1/A^\pm(p^2) &= 1/A(p^2) \pm \delta_3/[1 + (p^2/\kappa_2^2)^2], & \mathcal{M}^\pm(p^2) &= \mathcal{M}(p^2) \pm \delta_3/[1 + (p^2/\kappa_2^2)^2], \end{aligned} \quad (5.5)$$

with $\delta_1 = 0.16 \text{ GeV}^{-2}$, $\delta_2 = 0.03$, and $\delta_3 = 0.015 \text{ GeV}$, $\kappa_1^2 = 0.5 \text{ GeV}^2$, and $\kappa_2^2 = 2 \text{ GeV}^2$. With this choice of parameters, the infrared finite ingredients, Δ^\pm , $1/A^\pm$, and \mathcal{M}^\pm differ from their central values by $\sim 4\%$, within the interval $p \in [0, 1] \text{ GeV}$, while $L_{sg}^\pm(p^2)$, which diverges at the origin, shows the same variation for $p \in [0.1, 1] \text{ GeV}$. All $f^\pm(p^2)$ approaches $f(p^2)$ rapidly for $p \gtrsim 2 \text{ GeV}$.

The λ_1^{sg} resulting from performing each of the above variations is shown as a separate panel in Fig. 12; the inset in each case displays the ingredient being varied. In order to visually track the direction of the variations in λ_1^{sg} , the lower bound, f^- , of any given ingredient, and the λ_1 resulting from using this f^- , are marked with a dashed line. We note that λ_1^{sg} is enhanced when increasing Δ , L_{sg} , or the quark wave function, $1/A$. On the other hand, as expected, an increase in \mathcal{M} reduces λ_1^{sg} .

Since the numerically dominant non-Abelian diagram (see Sec. V A) is linear in $1/A$ and L_{sg} , but quadratic in Δ , we expect λ_1^{sg} to be especially sensitive to the gluon dressing function. Indeed, we observe in Fig. 12 that a variation of 4% in $1/A$ (L_{sg}) in the infrared region, has a 5% (3%) effect on $\lambda_1^{sg}(0)$. Moreover, λ_1^{sg} is rather insensitive to small variations of the constituent quark mass, \mathcal{M} , changing by only 1% in our tests. In contrast, enhancing

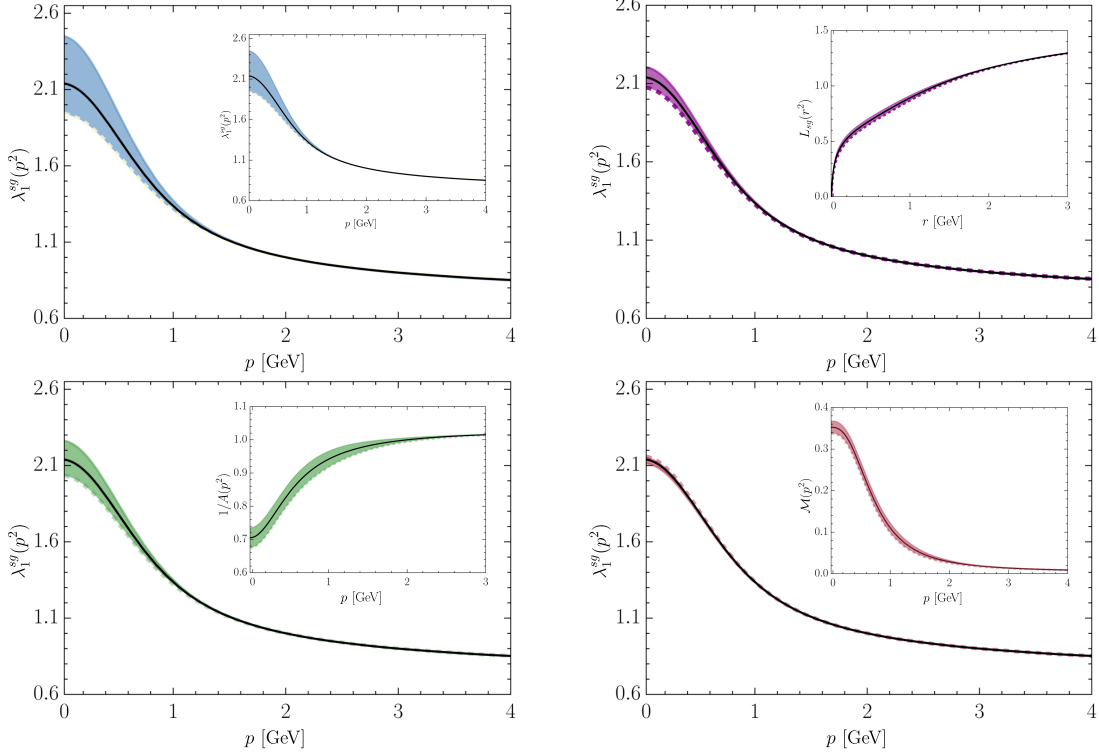


Figure 12. The effect of varying the inputs $\mathcal{Z}(q^2)$ (upper left), $L_{sg}(r^2)$ (upper right), $1/A(p^2)$ (lower left), and $\mathcal{M}(p^2)$ (lower right). The insets depict the corresponding variations, while the main plots show their impact on λ_1 .

Δ by the same 4% increases λ_1^{sg} by 14%.

Note finally that the above variations are uncorrelated, in contradistinction to what happens in a self-contained SDE analysis, where a change to one of them affects all others in complicated ways; nonetheless, we hope that the main tendencies are correctly captured.

E. Comparison with the lattice

In this subsection we compare our results for the quark-gluon vertex in the soft-gluon configuration with those obtained in the $N_f = 2$ lattice simulation of [61].

We first recall that in the soft-gluon limit, four out of the eight tensor structures given by (2.6) vanish identically. Upon setting $p_1 = p_2 = p$, the tensorial structure of the transversely-projected vertex, $\overline{\Pi}_\mu(0, p, -p)$, simplifies to Eq. (A8), where the vanishing of $\lambda_3^{sg}(p^2)$ has already been taken into account. From the analysis presented in the Appendix A, it is clear that, formally, the classical form factors of the SDE and the lattice are exactly

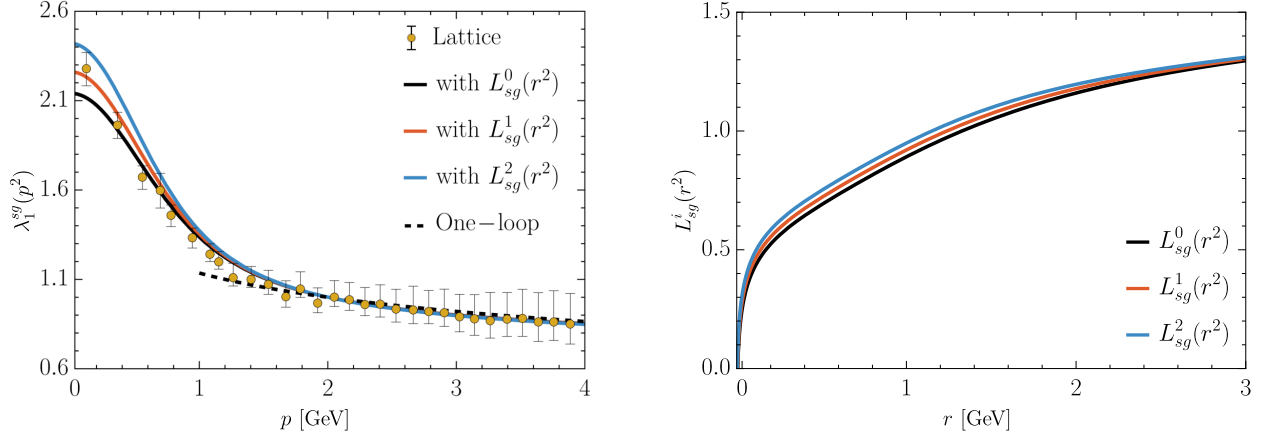


Figure 13. *Left panel:* Comparison of the form factor $\lambda_1^{sg}(p^2)$ in the soft-gluon configuration (continuous curves), computed with the $L_{sg}^i(r^2)$ shown in the right panel, with the “L08” lattice data (circles) of [61]. The one-loop result of [32] is shown as a black dashed line. *Right panel:* The $L_{sg}^i(r^2)$ given by Eq. (5.6) used to compute $\lambda_1^{sg}(p^2)$.

the same, *i.e.*, $\lambda_1^{sg}(p^2) = \lambda_1^L(p^2)$, as dictated by Eq. (A11).

In the left panel of Fig. 13, we compare the SDE result for the form factor $\lambda_1^{sg}(p^2)$, (black continuous curves) with the “L08” lattice data of [61] (circles). Evidently, both curves nearly coincide over most of the momentum range, showing a minor departure only in the deep infrared, where the corresponding saturation points differ by approximately 7%. Note that the value used in the SDE for obtaining this solution is $\alpha_s(\mu^2) = 0.55$. Finally, the black dashed line represents the one-loop result for $\lambda_1^{sg}(p^2)$ taken from [32], duly renormalized in the $\widetilde{\text{MOM}}$ scheme; we observe that both the SDE and lattice results recover the perturbative behavior for $p \gtrsim 2$ GeV.

Given the analysis of the previous subsection, it is clear that the coincidence between SDE and lattice may be easily improved even further, by introducing slight deviations in the inputs employed in the SDE. To demonstrate this possibility with a concrete example, let us allow for minor variations of the $L_{sg}(r^2)$ around $L_{sg}^*(r^2)$, using the same functional dependence as in Eq. (5.5).

In particular, we consider the family $L_{sg}^i(r^2)$, given by

$$L_{sg}^i(r^2) = L_{sg}^*(r^2) + \frac{\epsilon_i}{1 + (r^2/\kappa^2)^2}, \quad i = 0, 1, 2, \quad (5.6)$$

with $\epsilon_0 = 0$, $\epsilon_1 = 0.03$, $\epsilon_2 = 0.06$, and, $\kappa^2 = 5 \text{ GeV}^2$; the three curves are represented together in the right panel of Fig. 13. The resulting $L_{sg}^1(r^2)$ and $L_{sg}^2(r^2)$ clearly improve the

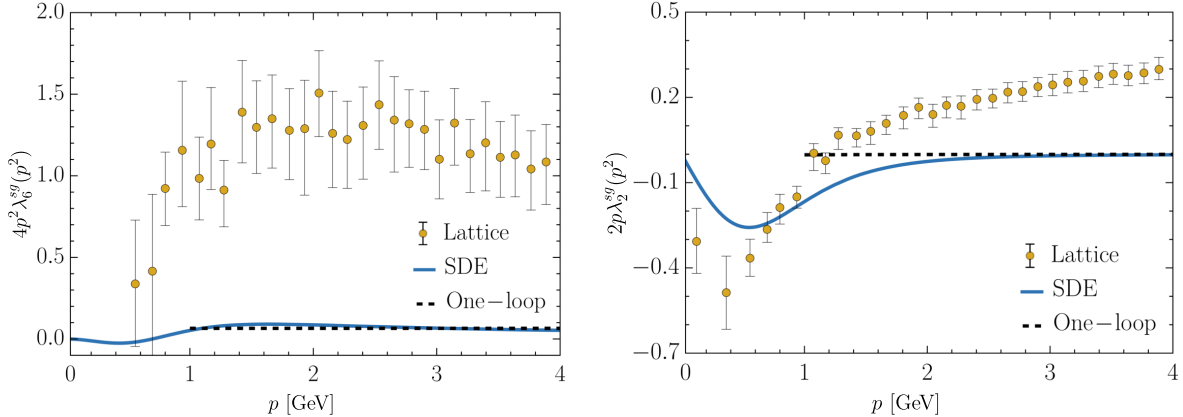


Figure 14. Comparison of the dimensionless soft-gluon form factors $4p^2 \lambda_6^{sg}(p^2)$ (left) and $2p \lambda_2^{sg}(p^2)$ (right) (blue continuous curves) with lattice data of [61] (circles). We also plot the corresponding one-loop results from [32] (black dashed curve).

overall coincidence with the lattice in the deep infrared. Similar levels of agreement may be obtained by varying the other inputs, in the spirit of Eq. (5.5); we will not pursue this possibility any further.

The excellent agreement found in the case of $\lambda_1^{sg}(p^2)$ between the SDE results and the lattice is in stark contrast to what happens with the remaining two form factors of the soft-gluon configuration. Specifically, using the formal correspondence $\lambda_6^{sg}(p^2) = \lambda_2^L(p^2)$ and $\lambda_2^{sg}(p^2) = \lambda_3^L(p^2)$ [see Eq. (A10)], in Fig. 14 we compare the typical dimensionless combinations $4p^2 \lambda_6^{sg}(p^2)$ and $2p \lambda_2^{sg}(p^2)$, observing strong qualitative discrepancies with respect to the lattice data of [61].

Historically, the lattice determination of the form factor $4p^2 \lambda_6^{sg}(p^2)$ [left panel of Fig. 14] has been rather problematic. In the quenched simulations of [58], $4p^2 \lambda_6^{sg}(p^2)$ appears to diverge at the origin, contrary to all continuous studies that yield a vanishing result [20, 36, 47, 48, 124]. Although the $N_f = 2$ simulation appears to have ameliorated this flaw, the ultraviolet tail of the data is clearly at odds with the correct one-loop perturbative behavior [32], shown as black dashed in Fig. 14. It would seem, therefore, that additional analysis is required before a meaningful comparison with the SDE results may be conducted.

Regarding $2p \lambda_2^{sg}(p^2)$, shown in the right panel of Fig. 14, we again observe a discrepancy between the lattice data and the expected one-loop behavior [32]. Although our result

for $2p\lambda_2^{sg}(p^2)$ exhibits a qualitative pattern similar to the unquenched lattice data [61], the minimum found in the deep infrared is considerably shallower than the one observed on the lattice.

It is worth stressing that the lattice $\lambda_2^{sg}(p^2)$ and $\lambda_6^{sg}(p^2)$ are known to be more severely affected by discretization artifacts than $\lambda_1^{sg}(p^2)$. Indeed, the “tree-level correction” procedure employed in [61], for the purpose of reducing discretization artifacts, improves significantly the agreement of $\lambda_1^{sg}(p^2)$ with its perturbative behavior. However, as explicitly stated in [61], it has the opposite effect on $\lambda_2^{sg}(p^2)$, pushing it away from its one-loop result at large momenta. Moreover, while for $\lambda_1^{sg}(p^2)$ and $\lambda_2^{sg}(p^2)$ the discretization artifacts are apparent mostly in the ultraviolet (see Figs. 4 and 6 of [61]), the aforementioned procedure affects $\lambda_6^{sg}(p^2)$ within the entire range of momentum (see Fig. 5 of [61]).

VI. VERIFYING MULTIPLICATIVE RENORMALIZABILITY

In this section we probe the veracity of multiplicative renormalizability at the level of the form factor $\lambda_1^{sg}(p^2)$. This exercise is particularly relevant in view of the subtractive nature of the renormalization procedure employed on the SDE derived from the 3PI effective action formalism, concretely Eqs. (4.6) and (4.7), as discussed in Sec. III B. The upshot of these considerations is that multiplicative renormalizability is faithfully reflected in the solutions of the SDE, essentially due to the fact that all vertices entering in diagrams a_μ and b_μ of Fig. 2 are fully dressed.

The main idea of our procedure is to repeat the calculation of λ_1 , with Eq. (4.6) renormalized in the same scheme, $\widetilde{\text{MOM}}$, but at a different renormalization point, to be denoted by ν , *i.e.*, imposing Eqs. (3.17) and (4.7) with $\mu \rightarrow \nu$. Then, if multiplicative renormalizability is respected, the two answers must be related by

$$\lambda_1^{sg}(p^2, \mu^2) = \frac{\lambda_1^{sg}(p^2, \nu^2)}{\lambda_1^{sg}(\mu^2, \nu^2)}. \quad (6.1)$$

In order to proceed, we need the inputs for $\Delta(q^2)$, $L_{sg}(r^2)$, and $A(p^2)$, shown in Figs. 3 and 4, respectively, at different renormalization points⁴. To obtain them, we will assume that multiplicative renormalizability is valid for these three functions, and use relations analogous to Eq. (6.1) to deduce their form at the new renormalization point.

⁴ Notice that the quark dynamical mass, $\mathcal{M}(p^2)$, is a μ -independent quantity, and therefore does not need to be rescaled.

Specifically, it follows from Eq. (3.13), and the fact that the unrenormalized Green's functions do *not* depend on the renormalization point, that

$$\begin{aligned}\Delta(q^2, \nu^2) &= \Delta(q^2, \mu^2) \frac{Z_A(\mu^2)}{Z_A(\nu^2)}, & A(p^2, \nu^2) &= A(p^2, \mu^2) \frac{Z_F(\nu^2)}{Z_F(\mu^2)}, \\ \lambda_1^{sg}(p^2, \nu^2) &= \lambda_1^{sg}(p^2, \mu^2) \frac{Z_1(\nu^2)}{Z_1(\mu^2)}, & L_{sg}(s^2, \nu^2) &= L_{sg}(s^2, \mu^2) \frac{Z_3(\nu^2)}{Z_3(\mu^2)}.\end{aligned}\quad (6.2)$$

Now, the values $\Delta(\nu^2, \nu^2)$, $A(\nu^2, \nu^2)$, and $\lambda_1^{sg}(\nu^2, \nu^2)$, are fixed by the renormalization prescription of Eq. (3.17) with $\mu \rightarrow \nu$. Hence, evaluating Eq. (6.2) at $q^2 = p^2 = \nu^2$ entails

$$\frac{Z_A(\mu^2)}{Z_A(\nu^2)} = \frac{1}{\nu^2 \Delta(\nu^2, \mu^2)}, \quad \frac{Z_F(\nu^2)}{Z_F(\mu^2)} = \frac{1}{A(\nu^2, \mu^2)}, \quad \frac{Z_1(\nu^2)}{Z_1(\mu^2)} = \frac{1}{\lambda_1^{sg}(\nu^2, \mu^2)}. \quad (6.3)$$

Then, substituting into Eq. (6.2) we obtain Eq. (6.1) with $\mu \leftrightarrow \nu$, together with

$$\Delta(q^2, \nu^2) = \frac{\Delta(q^2, \mu^2)}{\nu^2 \Delta(\nu^2, \mu^2)}, \quad A(p^2, \nu^2) = \frac{A(p^2, \mu^2)}{A(\nu^2, \mu^2)}. \quad (6.4)$$

On the other hand, the renormalization conditions of Eq. (3.17) do not specify the value of $L_{sg}(\nu^2, \nu^2)$. Instead, to determine $Z_3(\nu^2)/Z_3(\mu^2)$, we employ the fundamental relation $Z_3 = Z_1 Z_A / Z_F$, derived directly from Eq. (3.14), together with Eq. (6.3), which yield

$$\frac{Z_3(\nu^2)}{Z_3(\mu^2)} = \frac{\nu^2 \Delta(\nu^2, \mu^2) A(\nu^2, \mu^2)}{\lambda_1^{sg}(\nu^2, \mu^2)}, \quad (6.5)$$

and so,

$$L_{sg}(s^2, \nu^2) = \frac{\nu^2 \Delta(\nu^2, \mu^2) A(\nu^2, \mu^2)}{\lambda_1^{sg}(\nu^2, \mu^2)} L_{sg}(s^2, \mu^2). \quad (6.6)$$

The next step is to relate the values of $\alpha_s(\nu^2)$ and $\alpha_s(\mu^2)$, which we achieve by invoking the effective coupling $\widehat{g}_1^{sg}(p^2)$ of Eq. (5.1). Since $\widehat{g}_1^{sg}(p^2)$ is RGI, its value is the same when computed with ingredients renormalized at either μ or ν , *i.e.*,

$$\widehat{g}_1^{sg}(p^2) = \frac{g(\mu^2) \lambda_1^{sg}(p^2, \mu^2) \mathcal{Z}^{1/2}(p^2, \mu^2)}{A(p^2, \mu^2)} = \frac{g(\nu^2) \lambda_1^{sg}(p^2, \nu^2) \mathcal{Z}^{1/2}(p^2, \nu^2)}{A(p^2, \nu^2)}. \quad (6.7)$$

Therefore, setting $p = \nu$ in the above, using the renormalization prescription of Eq. (3.17) with $\mu \rightarrow \nu$, and $g^2 = 4\pi\alpha_s$, leads to

$$\alpha_s(\nu^2) = \alpha_s(\mu^2) [\lambda_1^{sg}(\nu^2, \mu^2)]^2 A^{-2}(\nu^2, \mu^2) \nu^2 \Delta(\nu^2, \mu^2). \quad (6.8)$$

Then, using the previously obtained curve for $\lambda_1^{sg}(p^2, \mu^2)$, shown in Fig. 13, together with the external inputs renormalized at $\mu = 2$ GeV, discussed in items (*i-iv*) of Subsec. IV C,

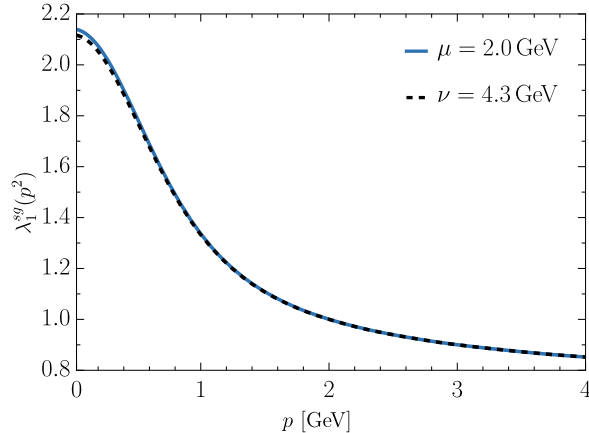


Figure 15. Verification that our solution for $\lambda_1^{sg}(p^2)$ satisfies the multiplicative renormalizability property given by Eq. (6.1).

we get all required inputs renormalized at $\nu = 4.3$ GeV through Eqs. (6.4), (6.6) and (6.8). In particular, we find $\alpha_s(\nu^2) = 0.28$.

With all the necessary inputs in hand, we solve Eqs. (4.6) and (4.7) again to obtain $\lambda_1(p^2, \nu^2)$ at $\nu = 4.3$ GeV. The result is then rescaled to $\mu = 2$ GeV using Eq. (6.1), and compared to the $\lambda_1(p^2, \mu^2)$ obtained by solving the SDE directly at μ . The comparison is shown in Fig. 15, where the blue continuous curve shows the result of the SDE renormalized at μ , whereas the black dashed corresponds to the solutions of the SDE renormalized at ν and subsequently rescaled to μ through Eq. (6.1). The nearly perfect coincidence of the two curves confirms that indeed multiplicative renormalizability is satisfied in our truncation.

VII. CONCLUSIONS

In the present work we have studied the transversely-projected quark-gluon vertex of QCD with two light degenerate quarks, in the Landau gauge. Our analysis is based on the SDE derived within the 3PI formalism at the three-loop level, where lattice results have been employed for all SDE components, except the quark-gluon vertex itself.

Under certain simplifying assumptions, we obtain all eight form factors, λ_i , of this vertex for arbitrary space-like momenta. Importantly, the classical form factor, λ_1 , exhibits a considerable angular dependence, displaying a large peak at the “asymmetric limit”, which is absent in the “soft-gluon” configuration (see Fig. 6). Moreover, our results confirm the hierarchy of the RGI effective couplings $\widehat{g}_i(p^2)$ found in the functional renormalization group

analysis of [10, 46], and the SDE study of [12]. In particular, $\widehat{g}_1^{sg}(p^2)$ is clearly dominant, its maximum value exceeding that of the second-largest $\widehat{g}_7^{sg}(p^2)$ by a factor of 3. In addition, in the soft-gluon limit, the comparison with the lattice results of [61] reveals excellent agreement for the classical form factor $\lambda_1^{sg}(p^2)$, and rather strong discrepancies for $\lambda_2^{sg}(p^2)$ and $\lambda_6^{sg}(p^2)$.

The aforementioned strong angular dependence of λ_1 precludes the possibility of accurately describing λ_1 in terms of a single variable, *e.g.*, $s^2 = (q^2 + p_1^2 + p_2^2)/2$, in contradistinction to the approximate “planar degeneracy” displayed by the form factors of the vertices with three (see Sec. IV A) and four-gluons [125, 126]. In hindsight, this difference appears natural, given that the planar degeneracy hinges crucially on the Bose symmetry of the vertex in question, which is clearly absent in the case of the quark-gluon vertex. To be sure, the analysis of [120], carried out under the hypothesis of planar degeneracy for the quark-gluon vertex, needs to be revisited, and the full kinematic dependence of $\lambda_1(q, p_2, -p_1)$ obtained here must be properly taken into account.

The numerical treatment in this work has been greatly simplified by decoupling the system of eight integral equations given in Eq. (4.6); in particular, the full dependence of all SDE kernels on λ_1 was maintained, while all other form factors were dropped. An evident improvement on the present analysis may be achieved by restoring the full dependence of the λ_i , and solving the resulting system of equations; calculations in this direction are already in progress.

It is especially challenging to couple the quark-gluon vertex to the gap equation of the quark propagator, and solve the resulting system self-consistently, maintaining the full kinematic structure of the λ_i . Evidently, such a treatment would determine dynamically the functions $A(p^2)$ and $\mathcal{M}(p^2)$, eliminating the need of using lattice inputs for them, as was done here. Within such a framework, one may explore the impact of the λ_i found in this work on the standard parameters describing dynamical chiral symmetry breaking, such as the constituent quark mass, the pion decay constant, and the light chiral condensate, see [12] and references therein. In fact, it would be interesting to study the effect that the pronounced angular dependence of λ_1 might have on chiral dynamics. We hope to be able to address some of these open issues in the near future.

VIII. ACKNOWLEDGMENTS

We thank Fei Gao and Jan Pawłowski for several useful interactions. The work of A. C. A. and G. L. T. is supported by the CNPq grants 310763/2023-1 and 131385/2022-4. A. C. A. also acknowledges financial support from project 464898/2014-5 (INCT-FNA). The work of B. M. O. was financed in part by the Coordenação de Aperfeiçoamento de Pessoal de Nível Superior - Brasil (CAPES) - Finance Code 00, and by the CNPq grants 141409/2021-5. M. N. F. acknowledges financial support from the National Natural Science Foundation of China (grant no. 12135007). J. P. is supported by the Spanish MICINN grant PID2020-113334GB-I00 and the Generalitat Valenciana grant CIPROM/2022/66. This research was performed using the Feynman Cluster of the John David Rogers Computation Center (CCJDR) in the Institute of Physics Gleb Wataghin, University of Campinas.

Appendix A: Transformation rules from Minkowski to Euclidean space

In this Appendix, we derive the relations between the form factors of the Minkowski tensor basis of Eqs. (2.5) and (2.6) and those of the direct Euclidean decompositions given by [10, 61].

As mentioned in the main text, the basis of Eq. (2.6) ensures, by construction, the equivalence between our form factors and those of [10], upon passing to Euclidean space. In [10], the Euclidean vertex, $\overline{\Pi}_\mu^E(q^E, p_2^E, -p_1^E)$, is decomposed directly as

$$\overline{\Pi}_\mu^E(q^E, p_2^E, -p_1^E) = \sum_{i=1}^8 \lambda_i^E(q^E, p_2^E, -p_1^E) P_{\mu\nu}(q^E) \tau_{iE}^\nu(p_2^E, -p_1^E), \quad (\text{A1})$$

with

$$\begin{aligned} \tau_{1E}^\nu(p_2^E, -p_1^E) &= \gamma_\nu^\nu, & \tau_{2E}^\nu(p_2^E, -p_1^E) &= i(p_1^E + p_2^E)^\nu, \\ \tau_{3E}^\nu(p_2^E, -p_1^E) &= i(\not{p}_1^E + \not{p}_2^E)\gamma_\nu^\nu, & \tau_{4E}^\nu(p_2^E, -p_1^E) &= i(\not{p}_2^E - \not{p}_1^E)\gamma_\nu^\nu, \\ \tau_{5E}^\nu(p_2^E, -p_1^E) &= (\not{p}_1^E - \not{p}_2^E)(p_1^E + p_2^E)^\nu, & \tau_{6E}^\nu(p_2^E, -p_1^E) &= -(\not{p}_1^E + \not{p}_2^E)(p_1^E + p_2^E)^\nu, \\ \tau_{7E}^\nu(p_2^E, -p_1^E) &= -\frac{1}{2}[\not{p}_1^E, \not{p}_2^E]\gamma_\nu^\nu, & \tau_{8E}^\nu(p_2^E, -p_1^E) &= -\frac{i}{2}[\not{p}_1^E, \not{p}_2^E](p_1^E + p_2^E)^\nu. \end{aligned} \quad (\text{A2})$$

To demonstrate that the basis above is the Euclidean equivalent of Eqs. (2.5) and (2.6), we follow the procedure described in [57].

We begin by contracting Eq. (2.5) from the right⁵ by the Minkowski Dirac matrix, γ^μ , and transforming the result to Euclidean space, to obtain $[\overline{\mathbb{I}}_\mu(q, p_2, -p_1)\gamma^\mu]_E$. Then, we verify that the result is the same as contracting Eq. (A1) by the Euclidian Dirac matrix, γ_E^μ , *i.e.*,

$$[\overline{\mathbb{I}}_\mu(q, p_2, -p_1)\gamma^\mu]_E = \overline{\mathbb{I}}_\mu^E(q, p_2, -p_1)\gamma_E^\mu. \quad (\text{A3})$$

For simplicity, we illustrate this procedure below by retaining only the contributions from the form factors λ_1 and λ_3 ; generalizing to the remaining λ_i is straightforward.

Contracting Eq. (2.5) from the right with γ^μ one obtains

$$\overline{\mathbb{I}}_\mu(q, p_2, -p_1)\gamma^\mu = (d-1) \left[\lambda_1(q, p_2, -p_1) + \lambda_3(q, p_2, -p_1)(\not{p}_1 + \not{p}_2) \right] + \dots, \quad (\text{A4})$$

where d is the spacetime dimension. Using the standard rules to convert the above result to Euclidean space [6], and requiring that the form factors do not change sign in the process, *i.e.*,

$$\not{p} \rightarrow i\not{p}_E, \quad p^2 \rightarrow -p_E^2, \quad \lambda_i(q, p_2, -p_1) \rightarrow \lambda_i^E(q^E, p_2^E, -p_1^E), \quad (\text{A5})$$

one gets that

$$[\overline{\mathbb{I}}_\mu(q, p_2, -p_1)\gamma^\mu]_E = (d-1) \left[\lambda_1^E(q^E, p_2^E, -p_1^E) - i\lambda_3^E(q^E, p_2^E, -p_1^E)(\not{p}_1^E + \not{p}_2^E) \right] + \dots. \quad (\text{A6})$$

An additional step may be required, depending on the conventions adopted for the Euclidean quark propagator. Applying Eq. (A5) to Eq. (2.14), we obtain $S_{0E}^{-1}(p_E) = i\not{p}_E - m_q$. However, [10] adopts the convention that $S_{0E}^{-1}(p_E) = i\not{p}_E + m_q$. These two conventions are related by the additional transformation $p_E \rightarrow -p_E$ [6], up to an overall sign that may be reabsorbed in the definition of the propagator. With this extra step, we obtain

$$[\overline{\mathbb{I}}_\mu(q, p_2, -p_1)\gamma^\mu]_E = (d-1) \left[\lambda_1^E(q^E, p_2^E, -p_1^E) + i\lambda_3^E(q^E, p_2^E, -p_1^E)(\not{p}_1^E + \not{p}_2^E) \right] + \dots. \quad (\text{A7})$$

The above result is exactly what we obtain when contracting the Euclidean form in Eq. (A1) with γ_E^μ from the right, establishing that Eqs. (A1) and (A2) is the Euclidean equivalent of Eqs. (2.5) and (2.6).

The same procedure can be applied in the soft-gluon configuration, to relate our form factors $\lambda_i^{sg}(p^2)$ with the $\lambda_j^L(p_E^2)$ computed on the lattice study of [61].

⁵ Since $\gamma_\mu \tau_7^\mu = 0$, contracting with γ_μ from the left leaves the Euclidean form of τ_7^μ undetermined.

Specifically, in the soft-gluon limit, Eq. (2.5) reduces to

$$\overline{\mathbb{I}}_{\mu}(0, p, -p) = \gamma_{\mu} \lambda_1^{sg}(p^2) + 2p_{\mu} \lambda_2^{sg}(p^2) + 4\not{p} p_{\mu} \lambda_6^{sg}(p^2). \quad (\text{A8})$$

Note that, although in this kinematic limit the tensor $\tau_3^{\nu}(p, -p) = 2\not{p}\gamma^{\nu}$ is non-zero, the associated form factor $\lambda_3^{sg}(p^2)$ vanishes due to charge conjugation symmetry, as discussed below Eq. (2.10).

Then, contracting Eq. (A8) with γ^{ν} , passing to Euclidean space through Eq. (A5), and using $p_E \rightarrow -p_E$ to account for the convention $S_{0E}^{-1}(p_E) = i\not{p}_E + m_q$ used in [61], yields

$$\left[\overline{\mathbb{I}}_{\mu}(0, p_E, -p_E) \gamma^{\mu} \right]_E = d\lambda_{1E}^{sg}(p_E^2) - 2i\not{p}_E \lambda_{2E}^{sg}(p_E^2) - 4p_E^2 \lambda_{6E}^{sg}(p_E^2), \quad (\text{A9})$$

where we note that the last equality in Eq. (A5) implies $\lambda_{iE}^{sg}(p_E^2) = \lambda_i^{sg}(-p_E^2)$.

Finally, substituting Eq. (A9) into Eq. (A3), it follows that the Minkowski basis for the soft-gluon kinematics in Eq. (A8) is equivalent to decomposing the vertex directly in Euclidean space as

$$\overline{\mathbb{I}}_{\mu}^E(0, p_E, -p_E) = \gamma_{\mu}^E \lambda_{1E}^{sg}(p_E^2) - 2i\not{p}_{\mu}^E \lambda_{2E}^{sg}(p_E^2) - 4\not{p}_{\mu}^E p_{\mu}^E \lambda_{6E}^{sg}(p_E^2). \quad (\text{A10})$$

The above is precisely the same as the basis used in the lattice study of [61], with the identification

$$\lambda_{1E}^{sg}(p_E^2) = \lambda_1^L(p_E^2), \quad \lambda_{6E}^{sg}(p_E^2) = \lambda_2^L(p_E^2), \quad \lambda_{2E}^{sg}(p_E^2) = \lambda_3^L(p_E^2). \quad (\text{A11})$$

-
- [1] W. J. Marciano and H. Pagels, *Phys. Rept.* **36**, 137 (1978).
 - [2] Y. Nambu and G. Jona-Lasinio, *Phys. Rev.* **122**, 345 (1961).
 - [3] Y. Nambu and G. Jona-Lasinio, *Phys. Rev.* **124**, 246 (1961).
 - [4] K. D. Lane, *Phys. Rev. D* **10**, 2605 (1974).
 - [5] H. D. Politzer, *Nucl. Phys. B* **117**, 397 (1976).
 - [6] C. D. Roberts and A. G. Williams, *Prog. Part. Nucl. Phys.* **33**, 477 (1994).
 - [7] P. Maris and C. D. Roberts, *Int. J. Mod. Phys. E***12**, 297 (2003).
 - [8] C. S. Fischer and R. Alkofer, *Phys. Rev. D***67**, 094020 (2003).
 - [9] A. C. Aguilar and J. Papavassiliou, *Phys. Rev. D***83**, 014013 (2011).

- [10] M. Mitter, J. M. Pawłowski, and N. Strodthoff, *Phys. Rev.* **D91**, 054035 (2015).
- [11] A. C. Aguilar, J. C. Cardona, M. N. Ferreira, and J. Papavassiliou, *Phys. Rev.* **D98**, 014002 (2018).
- [12] F. Gao, J. Papavassiliou, and J. M. Pawłowski, *Phys. Rev. D* **103**, 094013 (2021).
- [13] J. R. Lessa, F. E. Serna, B. El-Bennich, A. Bashir, and O. Oliveira, *Phys. Rev. D* **107**, 074017 (2023).
- [14] A. Bender, C. D. Roberts, and L. Von Smekal, *Phys. Lett.* **B380**, 7 (1996).
- [15] P. Maris and P. C. Tandy, *Phys. Rev.* **C60**, 055214 (1999).
- [16] A. Bender, W. Detmold, C. Roberts, and A. W. Thomas, *Phys. Rev.* **C65**, 065203 (2002).
- [17] A. Holl, A. Krassnigg, and C. D. Roberts, *Nucl. Phys. Proc. Suppl.* **141**, 47 (2005).
- [18] L. Chang and C. D. Roberts, *Phys. Rev. Lett.* **103**, 081601 (2009).
- [19] R. Williams, *Eur. Phys. J.* **A51**, 57 (2015).
- [20] R. Williams, C. S. Fischer, and W. Heupel, *Phys. Rev.* **D93**, 034026 (2016).
- [21] H. Sanchis-Alepuz and R. Williams, *Phys. Lett.* **B749**, 592 (2015).
- [22] G. Eichmann, H. Sanchis-Alepuz, R. Williams, R. Alkofer, and C. S. Fischer, *Prog. Part. Nucl. Phys.* **91**, 1 (2016).
- [23] M. Gomez-Rocha, T. Hilger, and A. Krassnigg, *Phys. Rev. D* **92**, 054030 (2015).
- [24] C. D. Roberts and S. M. Schmidt, *Prog. Part. Nucl. Phys.* **45**, S1 (2000).
- [25] J. Braun, L. M. Haas, F. Marhauser, and J. M. Pawłowski, *Phys. Rev. Lett.* **106**, 022002 (2011).
- [26] K. Fukushima and T. Hatsuda, *Rept. Prog. Phys.* **74**, 014001 (2011).
- [27] C. S. Fischer, *Prog. Part. Nucl. Phys.* **105**, 1 (2019).
- [28] W.-j. Fu, J. M. Pawłowski, and F. Rennecke, *Phys. Rev. D* **101**, 054032 (2020).
- [29] F. Gao and J. M. Pawłowski, *Phys. Rev. D* **102**, 034027 (2020).
- [30] J. S. Ball and T.-W. Chiu, *Phys. Rev.* **D22**, 2542 (1980).
- [31] A. Kizilersu, M. Reenders, and M. Pennington, *Phys. Rev.* **D52**, 1242 (1995).
- [32] A. I. Davydychev, P. Osland, and L. Saks, *Phys. Rev.* **D63**, 014022 (2001).
- [33] J. Gracey, *Phys. Rev. D* **90**, 025014 (2014).
- [34] J. A. Gracey, *Phys. Rev.* **D84**, 085011 (2011).
- [35] R. Bermudez, L. Albino, L. X. Gutiérrez-Guerrero, M. E. Tejeda-Yeomans, and A. Bashir, *Phys. Rev.* **D95**, 034041 (2017).

- [36] M. Bhagwat and P. Tandy, [Phys. Rev. **D70**, 094039 \(2004\)](#).
- [37] F. J. Llanes-Estrada, C. S. Fischer, and R. Alkofer, [Nucl. Phys. Proc. Suppl. **152**, 43 \(2006\)](#).
- [38] H. H. Matevosyan, A. W. Thomas, and P. C. Tandy, [Phys. Rev. **C75**, 045201 \(2007\)](#).
- [39] C. S. Fischer, [J. Phys. G **32**, R253 \(2006\)](#).
- [40] S.-X. Qin, L. Chang, Y.-X. Liu, C. D. Roberts, and S. M. Schmidt, [Phys. Lett. **B722**, 384 \(2013\)](#).
- [41] D. Binosi, L. Chang, J. Papavassiliou, S.-X. Qin, and C. D. Roberts, [Phys. Rev. **D95**, 031501 \(2017\)](#).
- [42] M. Hopfer, A. Windisch, and R. Alkofer, [PoS **ConfinementX**, 073 \(2012\)](#).
- [43] E. Rojas, J. de Melo, B. El-Bennich, O. Oliveira, and T. Frederico, [J. High Energy Phys. **10**, 193 \(2013\)](#).
- [44] M. Peláez, M. Tissier, and N. Wschebor, [Phys. Rev. D **92**, 045012 \(2015\)](#).
- [45] R. Alkofer, C. S. Fischer, F. J. Llanes-Estrada, and K. Schwenzer, [Annals Phys. **324**, 106 \(2009\)](#).
- [46] A. K. Cyrol, M. Mitter, J. M. Pawłowski, and N. Strodthoff, [Phys. Rev. **D97**, 054006 \(2018\)](#).
- [47] A. C. Aguilar, D. Binosi, D. Ibañez, and J. Papavassiliou, [Phys. Rev. **D90**, 065027 \(2014\)](#).
- [48] A. C. Aguilar, J. C. Cardona, M. N. Ferreira, and J. Papavassiliou, [Phys. Rev. **D96**, 014029 \(2017\)](#).
- [49] O. Oliveira, W. de Paula, T. Frederico, and J. P. B. C. de Melo, [Eur. Phys. J. C **79**, 116 \(2019\)](#).
- [50] L. Albino, A. Bashir, L. X. G. Guerrero, B. E. Bennich, and E. Rojas, [Phys. Rev. D **100**, 054028 \(2019\)](#).
- [51] C. Tang, F. Gao, and Y.-X. Liu, [Phys. Rev. D **100**, 056001 \(2019\)](#).
- [52] M. Q. Huber, [Phys. Rept. **879**, 1 \(2020\)](#).
- [53] L. Albino, A. Bashir, B. El-Bennich, E. Rojas, F. E. Serna, and R. C. da Silveira, [JHEP **11**, 196 \(2021\)](#).
- [54] A. Windisch, M. Hopfer, and R. Alkofer, [Acta Phys. Polon. Supp. **6**, 347 \(2013\)](#).
- [55] O. Oliveira, T. Frederico, and W. de Paula, [Eur. Phys. J. C **80**, 484 \(2020\)](#).
- [56] J. Skullerud, P. O. Bowman, and A. Kizilersu, in *5th International Conference on Quark Confinement and the Hadron Spectrum* (2002) pp. 270–272.
- [57] J. Skullerud and A. Kizilersu, [J. High Energy Phys. **09**, 013 \(2002\)](#).

- [58] J. I. Skullerud, P. O. Bowman, A. Kizilersu, D. B. Leinweber, and A. G. Williams, *J. High Energy Phys.* **04**, 047 (2003).
- [59] J. I. Skullerud, P. O. Bowman, A. Kizilersu, D. B. Leinweber, and A. G. Williams, *Nucl. Phys. Proc. Suppl.* **141**, 244 (2005).
- [60] H.-W. Lin, *Phys. Rev.* **D73**, 094511 (2006).
- [61] A. Kizilersü, O. Oliveira, P. J. Silva, J.-I. Skullerud, and A. Sternbeck, *Phys. Rev. D* **103**, 114515 (2021).
- [62] A. Kizilersu, D. B. Leinweber, J.-I. Skullerud, and A. G. Williams, *Eur. Phys. J.* **C50**, 871 (2007).
- [63] A. Sternbeck, P.-H. Balduf, A. Kizilersu, O. Oliveira, P. J. Silva, J.-I. Skullerud, and A. G. Williams, *PoS LATTICE2016*, 349 (2017).
- [64] J.-I. Skullerud, A. Kizilersü, O. Oliveira, P. Silva, and A. Sternbeck, *PoS LATTICE2021*, 305 (2022).
- [65] O. Oliveira, A. Kizilersu, P. J. Silva, J.-I. Skullerud, A. Sternbeck, and A. G. Williams, *Acta Phys. Polon. Supp.* **9**, 363 (2016).
- [66] O. Oliveira, T. Frederico, W. de Paula, and J. P. B. C. de Melo, *Eur. Phys. J.* **C78**, 553 (2018).
- [67] J. M. Cornwall, R. Jackiw, and E. Tomboulis, *Phys. Rev. D* **10**, 2428 (1974).
- [68] J. Cornwall and R. Norton, *Phys. Rev. D* **8**, 3338 (1973).
- [69] J. Berges, *Phys. Rev. D* **70**, 105010 (2004).
- [70] J. Berges, *AIP Conf. Proc.* **739**, 3 (2004).
- [71] M. C. A. York, G. D. Moore, and M. Tassler, *JHEP* **06**, 077 (2012).
- [72] M. E. Carrington and Y. Guo, *Phys. Rev. D* **83**, 016006 (2011).
- [73] G. Eichmann, R. Williams, R. Alkofer, and M. Vujanovic, *Phys. Rev.* **D89**, 105014 (2014).
- [74] M. N. Ferreira and J. Papavassiliou, *Particles* **6**, 312 (2023).
- [75] A. C. Aguilar, M. N. Ferreira, J. Papavassiliou, and L. R. Santos, *Eur. Phys. J. C* **83**, 549 (2023).
- [76] F. Pinto-Gómez, F. De Soto, M. N. Ferreira, J. Papavassiliou, and J. Rodríguez-Quintero, *Phys. Lett. B* **838**, 137737 (2023).
- [77] F. Pinto-Gómez, F. De Soto, and J. Rodríguez-Quintero, *Phys. Rev. D* **110**, 014005 (2024).
- [78] A. L. Blum, R. Alkofer, M. Q. Huber, and A. Windisch, *EPJ Web Conf.* **137**, 03001 (2017).

- [79] A. L. Blum, *Three-gluon vertex and quark-gluon vertex functions in the Landau gauge*, Ph.D. thesis, Graz U. (2017).
- [80] R. Alkofer, [Symmetry **15**, 1787 \(2023\)](#).
- [81] A. C. Aguilar, D. Binosi, D. Ibañez, and J. Papavassiliou, [Phys. Rev. **D89**, 085008 \(2014\)](#).
- [82] A. Blum, M. Q. Huber, M. Mitter, and L. von Smekal, [Phys. Rev. **D89**, 061703 \(2014\)](#).
- [83] A. L. Blum, R. Alkofer, M. Q. Huber, and A. Windisch, [Acta Phys. Polon. Supp. **8**, 321 \(2015\)](#).
- [84] M. Q. Huber, [Phys. Rev. D **93**, 085033 \(2016\)](#).
- [85] A. K. Cyrol, L. Fister, M. Mitter, J. M. Pawłowski, and N. Strodthoff, [Phys. Rev. **D94**, 054005 \(2016\)](#).
- [86] L. Corell, A. K. Cyrol, M. Mitter, J. M. Pawłowski, and N. Strodthoff, [SciPost Phys. **5**, 066 \(2018\)](#).
- [87] A. C. Aguilar, M. N. Ferreira, C. T. Figueiredo, and J. Papavassiliou, [Phys. Rev. **D99**, 094010 \(2019\)](#).
- [88] M. Q. Huber, [Phys. Rev. D **101**, 114009 \(2020\)](#).
- [89] J. Papavassiliou, A. C. Aguilar, and M. N. Ferreira, [Rev. Mex. Fis. Suppl. **3**, 0308112 \(2022\)](#).
- [90] N. Barrios, M. Peláez, and U. Reinosa, [Phys. Rev. D **106**, 114039 \(2022\)](#).
- [91] A. Athenodorou, D. Binosi, P. Boucaud, F. De Soto, J. Papavassiliou, J. Rodríguez-Quintero, and S. Zafeiropoulos, [Phys. Lett. **B761**, 444 \(2016\)](#).
- [92] A. G. Duarte, O. Oliveira, and P. J. Silva, [Phys. Rev. **D94**, 074502 \(2016\)](#).
- [93] P. Boucaud, F. De Soto, J. Rodríguez-Quintero, and S. Zafeiropoulos, [Phys. Rev. **D95**, 114503 \(2017\)](#).
- [94] M. Vujanovic and T. Mendes, [Phys. Rev. **D99**, 034501 \(2019\)](#).
- [95] A. C. Aguilar, F. De Soto, M. N. Ferreira, J. Papavassiliou, J. Rodríguez-Quintero, and S. Zafeiropoulos, [Eur. Phys. J. **C80**, 154 \(2020\)](#).
- [96] A. C. Aguilar, F. De Soto, M. N. Ferreira, J. Papavassiliou, and J. Rodríguez-Quintero, [Phys. Lett. B **818**, 136352 \(2021\)](#).
- [97] G. T. R. Catumba, O. Oliveira, and P. J. Silva, [PoS **LATTICE2021**, 467 \(2022\)](#).
- [98] L. von Smekal, R. Alkofer, and A. Hauck, [Phys. Rev. Lett. **79**, 3591 \(1997\)](#).
- [99] A. C. Aguilar, D. Binosi, and J. Papavassiliou, [Phys. Rev. **D78**, 025010 \(2008\)](#).
- [100] C. S. Fischer, A. Maas, and J. M. Pawłowski, [Annals Phys. **324**, 2408 \(2009\)](#).

- [101] A. C. Aguilar, C. O. Ambrósio, F. De Soto, M. N. Ferreira, B. M. Oliveira, J. Papavassiliou, and J. Rodríguez-Quintero, [Phys. Rev. D **104**, 054028 \(2021\)](#).
- [102] A. Cucchieri and T. Mendes, [PoS **LATTICE2007**, 297 \(2007\)](#).
- [103] A. Cucchieri and T. Mendes, [Phys. Rev. Lett. **100**, 241601 \(2008\)](#).
- [104] I. Bogolubsky, E. Ilgenfritz, M. Muller-Preussker, and A. Sternbeck, [PoS **LATTICE2007**, 290 \(2007\)](#).
- [105] I. Bogolubsky, E. Ilgenfritz, M. Muller-Preussker, and A. Sternbeck, [Phys. Lett. **B676**, 69 \(2009\)](#).
- [106] O. Oliveira and P. Silva, [PoS **LAT2009**, 226 \(2009\)](#).
- [107] O. Oliveira and P. Bicudo, [J. Phys. G **G38**, 045003 \(2011\)](#).
- [108] A. Cucchieri and T. Mendes, [Phys. Rev. **D81**, 016005 \(2010\)](#).
- [109] P. Boucaud, F. De Soto, K. Raya, J. Rodríguez-Quintero, and S. Zafeiropoulos, [Phys. Rev. **D98**, 114515 \(2018\)](#).
- [110] A. Ayala, A. Bashir, D. Binosi, M. Cristoforetti, and J. Rodríguez-Quintero, [Phys. Rev. **D86**, 074512 \(2012\)](#).
- [111] D. Binosi, C. D. Roberts, and J. Rodríguez-Quintero, [Phys. Rev. D **95**, 114009 \(2017\)](#).
- [112] O. Oliveira, P. J. Silva, J.-I. Skullerud, and A. Sternbeck, [Phys. Rev. D **99**, 094506 \(2019\)](#).
- [113] J. Taylor, [Nucl. Phys. B **33**, 436 \(1971\)](#).
- [114] A. Slavnov, [Theor. Math. Phys. **10**, 99 \(1972\)](#).
- [115] S. Aoki *et al.* (Flavour Lattice Averaging Group), [Eur. Phys. J. C **80**, 113 \(2020\)](#).
- [116] F. Gao and J. M. Pawłowski, [Phys. Lett. B **820**, 136584 \(2021\)](#).
- [117] N. Dupuis, L. Canet, A. Eichhorn, W. Metzner, J. M. Pawłowski, M. Tissier, and N. Wschebor, [Phys. Rept. **910**, 1 \(2021\)](#).
- [118] W. Celmaster and R. J. Gonsalves, [Phys. Rev. D **20**, 1420 \(1979\)](#).
- [119] A. Hasenfratz and P. Hasenfratz, [Phys. Lett. B **93**, 165 \(1980\)](#).
- [120] A. C. Aguilar, M. N. Ferreira, D. Ibañez, and J. Papavassiliou, [Eur. Phys. J. C **83**, 967 \(2023\)](#).
- [121] J. Berntsen, T. O. Espelid, and A. Genz, [ACM Trans. Math. Softw. **17**, 452 \(1991\)](#).
- [122] C. de Boor, *A Practical Guide to Splines* (Springer, New York, 2001).
- [123] M. Q. Huber and L. von Smekal, [J. High Energy Phys. **04**, 149 \(2013\)](#).
- [124] F. J. Llanes-Estrada, C. S. Fischer, and R. Alkofer, [Nucl. Phys. B Proc. Suppl. **152**, 43](#)

(2006).

[125] A. C. Aguilar, M. N. Ferreira, J. Papavassiliou, and L. R. Santos, [Eur. Phys. J. C](#) **84**, 676 (2024).

[126] A. C. Aguilar, F. De Soto, M. N. Ferreira, J. Papavassiliou, F. Pinto-Gómez, J. Rodríguez-Quintero, and L. R. Santos, [arXiv:2408.06135 \[hep-ph\]](#) (2024).